Coastal Engineering 205 (2026) 104932

Contents lists available at ScienceDirect

Coastal Engineering

journal homepage: www.elsevier.com/locate/coastaleng

Wave–current interactions within microtidal systems

Maurizio Brocchini *, Francesco Marini, Agnese Baldoni

Università Politecnica delle Marche, Department of Construction, Civil Engineering and Architecture (DICEA), Via Brecce Bianche 12, Ancona, 60131, AN, Italy

ARTICLE INFO

Keywords:
Sea-river interaction
Wave blocking
Compound flooding

ABSTRACT

This study presents the first structured and comprehensive analysis of wave–current interactions at microtidal river mouths, a topic often overlooked in estuarine flood studies. Using long-term observations and modeling from the Misa River (Italy), we reveal how opposing currents significantly alter incoming sea waves, through processes such as wave blocking, steepening, and infragravity wave upriver propagation, leading to increased flood risk and morphological changes. A key contribution of this work lies in the detailed physical analysis of wave–current interaction mechanisms, developed through a combined theoretical and observational approach. The superposition of opposing flows and wave fields modifies wave propagation, bottom boundary layer dynamics, sediment transport, and energy dissipation at river mouths. Observations at the Misa River from monitoring system showed a shift from frequent moderate floods to fewer but more intense events. This change triggered cyclical sediment dynamics and mouth bar reshaping, driven by alternating low-flow accumulation and flood-induced erosion. The upriver propagation of IGWs, typically linked to tidal forcing, was detected despite negligible tides, confirming the dominant role of wave–current interactions. These dynamics, also documented at other microtidal rivers (e.g., Rhône, Mississippi), govern key processes such as sediment transport, nearshore wave patterns, and compound flooding. When river floods coincide with high sea levels, due to storm surge or sea level rise, the extent of flooding can increase substantially, particularly in low-lying urban areas. We give evidence of such process through the results of a novel numerical analysis performed at the Misa River estuary. The paper is an elaboration of the keynote lecture given by the first Author on the same topic at the 38th International Conference on Coastal Engineering.

1. Introduction

Wave–current interactions play a fundamental role in estuarine and coastal dynamics, influencing hydrodynamic processes across a wide range of spatial and temporal scales. Estuarine cities are increasingly exposed to flood hazards that result from the interaction of marine and riverine forcings, a phenomenon that is further exacerbated by climate change (Lyddon et al., 2024; Bevacqua et al., 2020). These interactions can occur in the presence of either opposing or following currents, each exhibiting distinct physical mechanisms that shape wave propagation and energy distribution. However, while these interactions are often mentioned in studies, the combined effect of river discharge and sea waves at river mouths is still insufficiently understood from a fundamental point of view. This study addresses this gap by proposing an integrated interpretation of estuarine dynamics from the viewpoint of wave–current interaction. Through a detailed exploration of the involved physical processes, supported by both original observations and literature, we aim to highlight how wave–current interactions drive many estuarine phenomena, including flooding, sediment dynamics, and morphological evolution.

In this study, we first introduce the theoretical foundations governing wave behavior over both opposing and following currents. We subsequently focus our analysis on the opposing current case, as it is particularly relevant in microtidal environments, where it exerts a dominant influence on sea-river interactions. In contrast, in macrotidal systems, opposing and following currents contribute with comparable significance. Under average conditions, microtidal river mouths represent highly dynamic environments where the interplay between riverine and marine forcings continuously modifies estuarine morphology and hydrodynamics. A comprehensive understanding of these processes requires bridging the classical divide between river and coastal dynamics, as estuarine systems inherently integrate both influences. Under extreme conditions, wave–current interactions become critical in amplifying flooding hazards. In particular, the simultaneous occurrence of high river discharge and elevated sea levels, expected to become more frequent due to climate change (Bevacqua et al., 2019), can substantially increase the risk of compound flooding in low-lying estuarine areas (Muñoz et al., 2020; Zscheischler et al., 2020). To develop effective response and mitigation strategies, it is crucial

* Corresponding author.
E-mail address: m.brocchini@univpm.it (M. Brocchini).

https://doi.org/10.1016/j.coastaleng.2025.104932
Received 2 September 2025; Received in revised form 5 December 2025; Accepted 5 December 2025
Available online 12 December 2025

to pinpoint the fundamental mechanisms driving these interactions. Identifying and quantifying these key processes will enable a better prediction of flood dynamics and support the implementation of targeted adaptation measures. This paper investigates sea-river interactions at microtidal river mouths, with a specific focus on their role in exacerbating flooding risks.

The study has two main objectives: to identify the key signatures of wave–current interactions under opposing flow conditions and to assess how these interactions eventually lead to an increased risk of flooding in estuarine environments. In the second part of the paper, we present evidence from multiple case studies of river mouths in microtidal environments, highlighting the variability of wave–current interactions and their effects. A particular focus is given to the Misa River, where long-term monitoring has provided valuable insights into the interplay between sea forcing and fluvial dynamics, making it a representative test site for studying these processes. Observations made at this natural-scale laboratory are used to illustrate sea-river dynamics at river mouths and support theoretical findings discussed in the first part of the paper. For its characteristics, the Misa River was also chosen as a case study for the "Mitigation and Adaptation in Resilient Coastal and estUarine integrated unitS - MARCUS" project, focusing on wave–current interactions at river mouths. Preliminary results of the project are presented here, including an experimental study on wave blocking and a numerical analysis for the assessment of compound flooding, also considering the effect of climate change.

Among the variety of dynamic processes that govern these interactions, including river discharge, different wave modes (wind waves, infragravity waves), sediment transport, density-driven circulation, and atmospheric conditions (e.g. "atmospheric rivers"), in this study, we focus on the detailed mechanics of the interaction between river currents and wind-generated sea waves. To this aim, we provide a thorough analysis of these interactions, placing particular emphasis on wave blocking, drawing from both our own modeling and field observations, as well as from published literature. The interaction between river currents and wind-generated sea waves plays a central role in controlling key processes such as the transport of passive tracers (e.g., sediments and pollutants) (Roco et al., 2024; Baldoni et al., 2022; Zhang et al., 2021), the morphological evolution of river mouths (Baldoni et al., 2021; Gao et al., 2018; Zăinescu et al., 2021), and the flooding of adjacent low-lying estuarine areas (Wahl et al., 2015; Green et al., 2025). The focus of the study is on microtidal environments so that the influence of tidal forces can be deemed as secondary or negligible with respect to the effects of river current, storm surge levels, wind-generated sea waves and their interactions.

Beyond clarifying the main scope of the paper, we also briefly recall what we do not analyze in any details (as this would entail a significantly more extensive treatment). This is related with:

- the atmospheric forcing known as "Atmospheric Rivers", which can lead to extreme rainfall events over river catchments and related flooding (e.g. Sioni et al., 2023);
- density-related dynamics, like density stratification (e.g. Valle-Levinson, 2010), salt intrusion (e.g. Liu et al., 2019; Bellafiore et al., 2021) and evolution of turbidity maxima (e.g. Postacchini et al., 2023) at river mouths.

Building on the keynote lecture delivered by the first Author at the 38th International Conference on Coastal Engineering, this work provides a deeper exploration of sea-river interactions in estuarine environments, emphasizing their significance in the context of both present-day variability and future climate-driven changes.

2. Wave–current interaction

2.1. Space-uniform currents

In agreement with the most acknowledged original studies of wave–current interactions at sea, our analysis starts from the simplest conditions of a horizontally and vertically uniform current and moves to more complex conditions of horizontally-varying (refraction theory) and vertically-varying currents. In the simplest conditions of a horizontally and vertically uniform current, this equivalent to still water viewed from a reference frame moving with the current velocity, thus inducing a change in frequency by Doppler shift (Peregrine, 1976) according to:

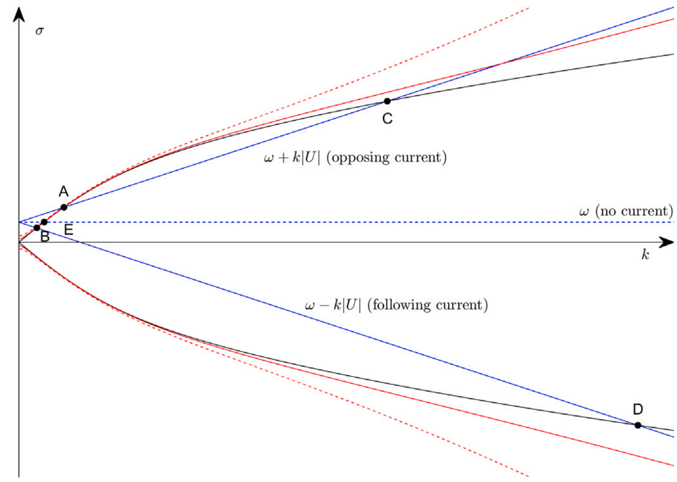

Fig. 1. Dispersion relation in the (k, σ) space (black line). Single solution for the waves only case (point E) and multiple solutions for waves with opposing current (points A and C) and waves with following current (points B and D). The red curves give the dispersion relation including nonlinear terms for small (continuous line) and larger (dashed line) wave heights.

$$\sigma = \omega - \mathbf{U} \cdot \mathbf{k} \tag{1}$$

where σ is the wave frequency relative to current, ω is the wave angular frequency, $\mathbf{U}$ is the current velocity, $\mathbf{k}$ is the wavenumber and the symbol $\langle\cdot\rangle$ represents the dot product. The wave celerity (C_ω), the wave celerity relative to the current (C_σ) and the wave group celerity (C_g) can be computed as:

$$C_\omega = \omega/k; \quad C_\sigma = \sigma/k; \quad C_g = \frac{d\sigma}{dk} \tag{2}$$

The Doppler shift is such that the dispersion relation for linear waves becomes:

$$(\omega - \mathbf{U} \cdot \mathbf{k})^2 = \sigma^2 = gk \tanh kh \tag{3}$$

where h is the water depth and g is the gravitational acceleration. Eq. (3) allows for multiple solutions obtained by intersecting the plane $\omega - \mathbf{U} \cdot \mathbf{k}$ with the surface of revolution $\pm\sigma = \pm\sqrt{gk \tanh kh}$ in the $(\mathbf{k}, \sigma)$ space (Peregrine and Jonsson, 1983). Fig. 1 illustrates this for the collinear case ($\mathbf{U} \cdot \mathbf{k} = Uk$) and for $k > 0$ (positive wave direction). In case of waves only ($U = 0$) the wavelength (L) is obtained from the dispersion relation (case E in Fig. 1).

When a current is added, two different solutions are obtained, for short and long waves, respectively. The long wave solutions, associated to the smaller values of k (points A and B in the Figure), close to point E, are the first met by increasing the slope U, while points C and D are the solutions associated to shorter waves (larger values of k). Among the long wave solutions, an opposing current decreases the wavelength; point A is associated to a larger value of k. On the contrary, for a following current (point B) an increase in wavelength is obtained due to the smaller value of k.

Focusing on the opposing current situation, if small values of $|U|$ are considered, cases A and C can be obtained. The wave group celerity of Eq. (2), can be seen as the slope of the dispersion relation curve in Fig. 1. Recalling that $C_\omega \geq C_g$ regardless of the water depth, case A corresponds to the situation in which $C_\omega \geq C_g > |U|$. This means that both single waves and energy propagate upstream overcoming the current. For case C which only exists for small enough waves (for larger waves the intersection C does not occur, see also Section 2.1.2), the condition $C_g \le |U|$ is achieved. In this case, wave energy is swept downstream by the current as also single waves in shallow water conditions ($C_\omega = C_g$). Since the energy flux for waves C_ω is directed downstream, these waves must be generated upstream from where they are present (Suastika, 2004). They represent waves reflected at the blocking point, where they have the same wavelength as the incident waves (A=C). Moving downstream the current weakens, so that C shifts to larger wavenumber (the reflected waves shorten). The A=C condition is associated to $C_g = |U|$, here the wave blocking condition is achieved due to the effect of the current velocity that blocks the upstream propagation of the wave energy, thus inducing also reflection (relatively small waves) or breaking (large enough waves). For larger values of the current velocity no waves propagate against the current. An interesting example of intense wave blocking is that occurring at Seymour Narrows (British Columbia, Canada). There, the tidal current entering the Narrows is accelerated because flowing N-S across a very narrow gap (750 m) between the Vancouver Island and the mainland. The result is an extremely fast current that blocks the opposing (S-N) waves and can also sweep them back (www.youtube.com/watch?v=yVW6XclyBak).

Since the 1980's, several authors studied the influence of the currents on water waves. Brevik (1980) experimentally studied wave–current interaction in a flume. His studies were mainly conducted in intermediate waters ($h/L \approx 0.13$) where the typical "deep water" behavior was observed with nonlinear waves ($0.33 < \varepsilon < 0.60$), being ε the wave nonlinearity ($\varepsilon = H/h$), and a uniform current profile ($U = 37$ cm/s). His results showed that the opposing current reduces the wavelength and, being the energy transfer limited, the wave becomes higher and more skewed. The opposite behavior is found for a following current. Wave amplitude dispersion is disregarded while frequency dispersion is very strong. Such behavior is only observed in deep to intermediate waters, where the importance of the main nonlinear effects is relative. For this reason, the following sections are aimed at understanding the effects due to nonlinear triad interaction (Section 2.1.1) and wave amplitude dispersion (Section 2.1.2).

2.1.1. Triad interaction

The behavior of the wavelength can be considered independent from both wave nonlinearity (ε) and depth regime (h/L), increasing for a following current and decreasing for an opposing current. Unlike that, the wave height (H) undergoes a more complex behavior because of the mode-mode interactions between wave components depending on the phase mismatch (δ_k) between triads. Triad interactions occur among waves with angular frequencies and wavenumbers such that:

$$\omega_1 \pm \omega_2 = \omega_3 \tag{4}$$

$$k_1 \pm k_2 = k_3 \tag{5}$$

This means that if component 3 satisfies the linear dispersion relation, the interaction is resonant and a one-way transfer of energy from components 1 and 2 to component 3 is obtained (Armstrong et al., 1962). This condition is achieved in very shallow waters when waves are nondispersive and their wavenumber only depends on water depth. For nearly shallow waters, component 3 does not satisfy the dispersion relation, the interaction is quasi-resonant and the transfer of energy can go back-and-forth because of the mismatch in the phase speed (Phillips, 1960; Hasselmann, 1962). The difference between the expected resonant wavenumber and the actual wavenumber at frequency ω_3 gives rise to a wavenumber mismatch defined as:

$$\delta_k = |k_1 \pm k_2| - k_3(\omega_3) \tag{6}$$

Such mismatch represents the distance from the exact resonance and it determines the intensity of the energy exchange between wave components. A zero mismatch is only obtained in very shallow waters and implies a one-way transfer of energy (resonant interaction) over a short evolution distance. For weakly dispersive waves ($\delta_k \ll 1$), a small variation of phase relations between waves occurs, thus inducing a significant net energy transfer over several wavelengths. In deep waters, waves are strongly dispersive, phase relations vary rapidly and a negligible energy transfer between wave components occurs. A more detailed and comprehensive discussion on nonlinear wave interactions can be found in Eldeberky (1997).

The presence of a current on waves also influences the interaction between triads, due to its influence on the dispersion relation given in Eq. (3). Fig. 1 shows that an opposing current increases the wavenumber and reduces the wavelength (from point E to A). In this case, the relative depth (h/L) increases, thus increasing the phase mismatch and reducing the amount of energy transfer between harmonics moving away from the shallow water condition. On the contrary, a following current increases the wavelength (point B) and the resulting waves propagate in relatively shallower depths where the phase mismatch is smaller and interactions are stronger.

The presence of higher harmonics increases with respect to what is expected for the no current case as also observed by Chen et al. (1999). In their study, a 3rd order Stokes wave ($\varepsilon = 0.2$) propagates in nearly-shallow waters ($h/L = 0.08$) with a current of $U/\sqrt{gh} = 0.15$. They found that, for the following current case, the phase mismatch lengthens the beatlength by 86% and increases the second harmonic amplitude by 20%. The opposite behavior is found for the opposing current case, in which a reduction of 57% in beat-length and of 14% in the second harmonic amplitude is observed. This mechanism has an important effect on the overall wave height. Numerical experiments of Kumar and Hayatdavoodi (2023) show that the mode-mode interactions lead to a wave height behavior in shallow waters ($h/L = 0.01$ and $0.2 < \varepsilon < 0.4$) opposite to that occurring in deep waters. The wave component at the primary frequency (H_1) is found to behave like in the deep water conditions (e.g. increasing/decreasing for opposing/following current, respectively). However, the first harmonic (H_2) is mainly influenced by mode-mode interactions and its amplitude shows a decrease for opposing current and an increase for following current. Given the large relative importance of super-harmonics in shallow waters, the overall wave height follows the behavior of its first harmonic, highlighting the importance of triad interaction over linear dispersion in this situation.

2.1.2. Wave amplitude dispersion

Another nonlinear effect that must be taken into account when studying the interaction between current and waves at the wave blocking condition is amplitude dispersion. It is well known that larger waves propagate with higher celerity and this effect can be taken into account by using a higher-order dispersion relation such us the one given in Chawla and Kirby (2002) for 3rd order Stokes waves:

$$\sigma = \sqrt{gk\tanh(kh)\left[1 + (ka)^2\left(\frac{8 + 4\cosh 4kh - 2\tanh^2 kh}{8\sinh^4 kh}\right)\right]} \tag{7}$$

where a is the wave amplitude. Such nonlinear dispersion relation can be represented in the $k - \sigma$ plane by the two red curves, computed for a lower (continuous line) and a higher (dashed line) value of wave amplitude. Its main effect on wave–current interaction refers to the wave reflection condition for the opposing current case (point C in Fig. 1). In particular, for increasing values of wave height, the reflection condition (second intersection between the nonlinear dispersion relation and the $\omega + k|U|$ line) moves to higher values of k. This means that the wavelength of reflected waves is reduced for increasing wave height. A further increase in wave height (red continuous line), can lead to the reversal of the concavity of $\sigma(k)$ and the reflection condition, in which both energy and waves are swept by the current, is not achieved.

The experiments of Chawla and Kirby (2002) were run for nonlinear waves ($0.066 < \varepsilon < 0.282$ in intermediate waters ($0.26 < h/L < 0.37$) against a uniform current with $U = 0.53$ m/s and they found that nonlinear effects of amplitude dispersion are only important close to wave blocking or wave breaking.

2.2. Horizontally varying currents (refraction theory)

In most common cases, the current velocity is not uniformly distributed along its section. As an example, focusing on estuarine dynamics, river plumes assume different shapes (e.g. arched, elongated, trapped) immediately after exiting the river mouth (Garvine, 1995; Yankovsky and Chapman, 1997; Osadchiev and Zavialov, 2019; Baldoni et al., 2022). The condition of the horizontal variation of the current can be described by the wave ray theory (Peregrine, 1976; Chao, 1993), with the assumptions that (i) the wave phase $\mathbf{k} \cdot \mathbf{x} - \omega t$ is a smooth function and (ii) waves are small. The wave action (A), of wave action flux (B) and of wave angular frequency (ω) are defined as follows

$$A = E/\sigma = \frac{1}{2}\frac{\rho g a^2}{\sigma} \qquad \mathbf{B} = (\mathbf{U} + \mathbf{C_g})A \qquad \omega = \mathbf{U} \cdot \mathbf{k} + \sigma(k, h) \tag{8}$$

where E is the wave energy and a is the wave amplitude. Given these definitions, the Ray equations can be written as (e.g. Peregrine, 1976; Peregrine and Jonsson, 1983):

$$\left[\frac{\partial}{\partial t} + (\mathbf{U} + \mathbf{C_g}) \cdot \nabla\right] k_i = -\frac{\partial \sigma}{\partial h}\frac{\partial h}{\partial x_i} - k_j \frac{\partial U_j}{\partial x_i} \tag{9}$$

$$\left[\frac{\partial}{\partial t} + (\mathbf{U} + \mathbf{C_g}) \cdot \nabla\right] \omega = \frac{\partial \sigma}{\partial h}\frac{\partial h}{\partial t} + k_j \frac{\partial U_j}{\partial t} \tag{10}$$

$$\left[\frac{\partial}{\partial t} + (\mathbf{U} + \mathbf{C_g}) \cdot \nabla\right] A + \left[\nabla \cdot (\mathbf{U} + \mathbf{C_g})\right] A = 0 \tag{11}$$

Eqs. (9) and (10) are used to trace wave rays, while Equation (11), expressing the conservation of wave action between rays, is used to compute the wave amplitude.

Simple refraction due to underwater topography occurs when the water depth h changes in time and space, as expressed by the first terms on the right-hand side of Eqs. (9) and (10). In this case, the orthogonals to the wave crests (i.e., lines parallel to $\mathbf{k}$) represent the direction of wave travel. In the presence of a current (not parallel to waves), the ray direction differs from the direction of the wavenumber vector, thus rays are not orthogonal to wave crests. Wave rays are in the direction of travel of the absolute group velocity (equal to the vector sum of current and the relative group velocity). For a nonzero angle between the wavenumber vector and the current a change in current leads to some refraction of the waves (Peregrine, 1976). The effect of a horizontally and temporally varying current can be observed from Eqs. (9) and (10), respectively: when waves propagate onto a faster or slower flow, ω remains constant, but L either increases or decreases; on the other hand, if the flow accelerates or decelerates, ω increases or decreases, the Doppler effect.

As a simple example, one can consider a current $U = U(x)$, describing a flow in channels and rivers where the velocity varies in response to the depth $h(x)$ and slope of the bottom. If waves travel parallel to the current, it is $\mathbf{U} \cdot \mathbf{k} = \pm U k$. Since the current is steady, ω along rays remains constant (Eq. (9)). Further, conservation of the wave action (Eq. (11)) implies that the wave action flux B is also constant, so that if $U + C_g$ approaches zero, which means the wave blocking condition is reached, the wave amplitude unrealistically increases: the analytical solution by wave action conservation fails at the blocking point, prescribing a divergent amplitude. Such singularity in amplitude has led to the assumption that waves break before reaching the blocking velocity (Peregrine, 1976). This is true for sufficiently steep waves, but the case can also occur in which waves are reflected in the vicinity of the blocking point, as shorter waves, and rapidly decay. In such situation, the phase velocity is directed upstream while energy transport velocity is directed downstream (Suastika, 2004). This happens because the blocking point corresponds to a caustic of rays and there is a set of rays being swept downstream (Peregrine and Jonsson, 1983).

Many experimental tests have been performed to observe wave blocking by an adverse current. Suastika (2004) tested both periodic and random waves traveling towards a current. He found that incident waves shorten and steepen as they advance on the adverse current, consistent with theoretical predictions. If the steepness exceeds a maximum value ($H \approx 0.1L$), waves may break on the adverse current, with the rear face being steeper than the forward one, contrary to what happens during depth-induced wave breaking (Peregrine and Jonsson, 1983). In the experiments, wave reflection due to blocking was also observed: the water surface became corrugated due to shortened reflected waves propagating downstream from the blocking point. The surface pattern on incident and reflected waves does not show a clear structure of nodes and antinodes like for the case of simple reflection due to a vertical wall.

These results were observed for both periodic and random waves. Moreover, random wave tests allowed to capture the narrowing of the wave spectra, as higher-frequency components got blocked by the current, and the shift of the spectral peak to lower frequencies. For a partial blocking, such shift did not occur (Suastika, 2004).

Chen et al. (1998) simulated monochromatic linear waves ($\varepsilon < 0.023$) propagating against a current in a channel with a submerged bar, i.e. from deep waters ($h/L = 0.53$) to intermediate waters ($h/L = 0.12$). They observed both amplitude increase and wavelength reduction approaching the blocking point, in agreement with the theoretical solution obtained by the principle of wave action. Again, such theory fails close to the blocking point, since in reality the wave amplitude does not go to infinity. As previously discussed, waves are either reflected back or break. When bichromatic waves are considered, the longer mode continues to propagate upstream of the blocking location, leading to frequency downshifting.

2.3. Vertically varying currents (shearing effects)

The vertical variation of the velocity profile plays a critical role in characterizing the dynamics of the flow. When waves interact with currents, the velocity distribution within the water column deviates significantly from that of a purely wave-driven or current-driven flow. These deviations arise from the complex interplay of forces at the boundaries, including the influence of surface waves, the frictional interaction at the seabed, and the turbulent processes within the fluid. Understanding these vertical velocity profiles is essential for predicting the transport of momentum, energy, and mass in natural and engineered aquatic systems.

There are two primary cases of interest: (1) wind stresses acting at the surface and (2) frictional stresses exerted at the bottom (Peregrine, 1976). The transfer of momentum from these boundary forces into the fluid body is mediated through a combination of viscous stresses, which dominate in regions of laminar flow, and turbulent Reynolds stresses, which become significant in turbulent regions. As noted by Umeyama (2005), the turbulent Reynolds stresses play a critical role in shaping the Eulerian-mean velocity profile. Umeyama (2005) observed that for a mean current velocity of approximately 12 cm/s, the wave height decreases in both following and opposing wave–current scenarios, reflecting a dynamic redistribution of energy. For waves propagating in the same direction as the current, the mean velocity near the free surface is reduced when compared to the logarithmic velocity profile typical of current-only conditions. Conversely, in cases where waves oppose the current, the mean velocity near the free surface is enhanced relative to the logarithmic profile. These effects underscore the nonlinear nature of wave–current interactions and the importance of accounting for turbulent stresses in the analysis. Building upon the understanding of vertical velocity profiles in wave–current interactions, laboratory experiments have provided valuable insights into the complex dynamics involved.

Kemp and Simons (1982) conducted experimental studies in a laboratory channel with both rough and smooth beds, investigating the interaction between gravity waves and a following turbulent current. For a flow depth of approximately 20 cm and a mean velocity of 18.3 cm/s, their findings demonstrated that the boundary layer (BBL)

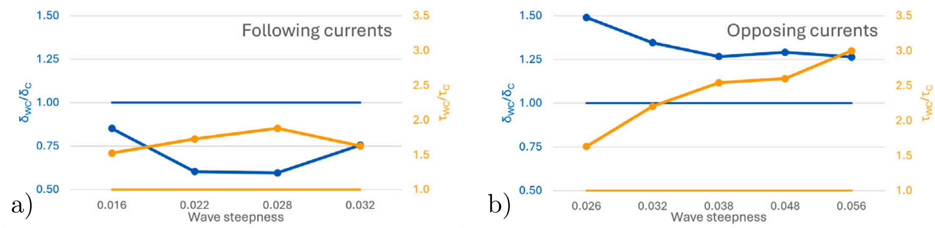

Fig. 2. Effect of waves over a current in terms of BBL thickness and bottom shear stress. Panel a: following current; Panel b: opposing current.
Source: Adapted from Kemp and Simons (1982, 1983).

thickness (δ) is reduced in the presence of following waves, with the mean velocity below the wave trough level decreasing. This phenomenon was attributed to the enhanced energy dissipation of larger wave heights, which transfers energy into the current. Above the BBL, the mean flow velocity was observed to increase, resulting in a deviation from the expected logarithmic profile. Shear stresses at the smooth boundary adhered to a linear combination of wave and current effects, indicating the persistence of superposition principles in certain stress mechanisms.

In their subsequent study, Kemp and Simons (1983) investigated the interaction between waves and an opposing current under similar experimental conditions. They observed that the boundary-layer thickness increases in the presence of opposing waves, with a notable amplification of the mean flow velocity below the wave trough level. This adjustment was accompanied by an increased decay rate of wave height in space, faster for opposing currents compared to following ones. Turbulence levels near the bed were significantly amplified, particularly in a layer approximately two roughness heights above the bed, where periodic vortex ejections contributed to elevated Reynolds stresses. Beyond this layer, turbulence levels over the smooth bed were comparable to current-only conditions, indicating a reduced influence of the opposing waves further away from the boundary.

The main findings obtained for both following and opposing currents by Kemp and Simons (1982, 1983) are illustrated in Fig. 2.

Here, the effect of the waves over an existing current is shown in terms of BBL thickness and bed friction (τ). In this figure, the subscript wc refers to the wave plus current test while c refers to the current only test. The bed friction by interacting nonlinear waves and currents is always larger than that due to currents alone, and for opposing currents is larger than for following currents and it increases with wave steepness. However, conditions exist for which the wall shear stress due to waves and currents is smaller than those of current alone ($\tau_{wc} < \tau_c$) (Lodahl et al., 1998). This occurs when waves can re-laminarize the current, i.e. the combined flow is wave dominated ($U_w \gtrsim U$) and the oscillatory component of the flow is in the laminar flow regime ($Re_w < 1.5 \cdot 10^5$). All the above has important bearings of sediment mobility and transport.

The wave-induced stresses, are also responsible for the deviations from the logarithmic profile. Huang and Mei (2003) have shown analytically that the near-surface velocity of an otherwise uniform current is reduced by following waves, but is increased by opposing waves as the consequence of second order effects of wave–current interaction. The mean velocity profile $\overline{U(z)}$ deviates from the logarithmic profile due to wave-induced stresses, as described by the following compact equation, adapted from Huang and Mei (2003):

$$\overline{U(z)} = \frac{U_*}{\kappa} \ln\left(\frac{z}{z_r}\right) + \int_\delta^z (\tau_{\upsilon_T} \pm \tau_{\alpha_c} + \tau_{E_D} + \tau_B + \tau''_{\upsilon_T}) dz \tag{12}$$

where U_* is the friction velocity, κ is the von Kàrmàn constant and z_r is the roughness height. The other terms represent different wave-induced shear stress contributions such as:

- τ_{υ_T} represents the distortion of the vertical profile of the eddy viscosity (υ_T) by free surface oscillation. This term is the most significant; it is always negative and it is large at surface;
- τ_{α_c} is the wave-induced change of friction velocity. Positive sign for following current, negative sign for opposing and nul at the surface;
- τ_{E_D} is the wave damping which is always positive and large at surface;
- τ_B is the wave-induced Reynolds stress from BBL. it is always negative and large at surface. It typically cancels out τ_{E_D};
- τ''_{υ_T} is the curvature of eddy viscosity which is always positive and large at surface.

For following currents, negative stresses decrease surface current velocity and positive stresses increase it. For opposing currents, negative stresses increase surface current velocity and positive stresses decrease it. This boundary-layer analysis with depth-dependent eddy viscosities allowed to explain the velocity profile experimentally observed by other authors (Kemp and Simons, 1982, 1983). For opposing currents, a reduction in velocity near the bottom and an increase near the surface, relative to the logarithmic current-only profile, are accurately predicted for the mean velocity. The opposite behavior is observed for following currents.

The same problem was investigated by Tambroni et al. (2015) using a perturbation approach, which assumes small wave steepness and considers current velocities to be of the same order of magnitude as the amplitude of velocity oscillations induced by wave propagation. The proposed model is relatively simple and supported by experimental measurements. At the leading-order approximation, wave–current interaction occurs primarily within the BBL due to the small ratio of boundary layer thickness to wavelength. At second order, waves alter the mean current profile through the momentum flux induced by velocity oscillations. As noted by Huang and Mei (2003), the resulting mean shear stresses near the free surface oppose the direction of wave propagation, leading to a reduction in mean current for following waves and an increase for opposing waves. Both the works of Huang and Mei (2003) and Tambroni et al. (2015) focused on the core region and on the bottom boundary layer.

Olabarrieta et al. (2010) developed a numerical model to include the variation of the free surface elevation due to the wave motion, in order to extended the analysis in the area the wave crest and trough. They confirmed the presence of a surface boundary layer in the upper part of the water column, which influences the flow structure throughout the entire water column. Between the wave crest and trough, the flow increases in the following cases and decreases in the opposing ones. This behavior is driven by the Stokes drift, the wave-induced mass flux in the direction of wave propagation.

As a summary, a qualitative sketch of the vertical velocity profile for following/opposing currents is reported in Fig. 3. These results highlight the intricate interplay between wave-induced and current-driven forces and their role in shaping the velocity profiles and stress distributions in wave–current interactions. Together with the observations of Umeyama (2005), they emphasize the critical influence of

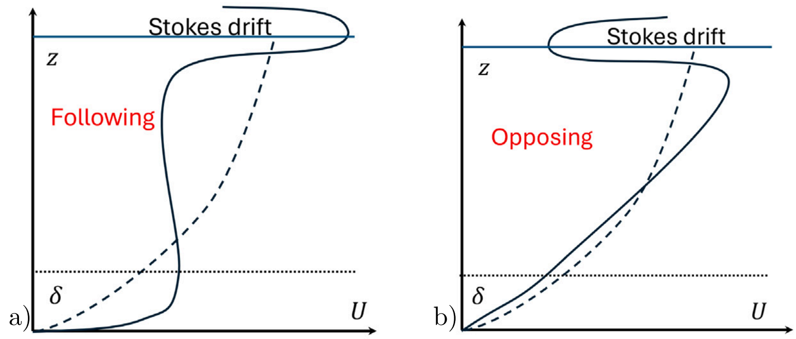

Fig. 3. Qualitative velocity profile in combined wave and current condition. The dashed line represents the reference logarithmic profile for current only conditions. Panel a: following current; Panel b: opposing current.

wave directionality on boundary-layer dynamics and the redistribution of momentum and energy within the water column.

2.4. Wave blocking

A strong opposing current can partially or completely block wave propagation in a specific condition. The current can block the upstream wave energy propagation if when its velocity is equal to waves' group celerity (condition A=C in Fig. 1). The blocking condition is obtained when the line and the curve in $k-\sigma$ plane are tangent (see Fig. 1). Such condition occurs when the curve and the line pass through the same point and have the same derivative, according to the following equations:

$$|U| = C_g = \frac{d\sigma}{dk} = n(k)C_\sigma = n(k)\frac{\sigma(k)}{k} \tag{13}$$

$$\omega + k|U| = \sigma(k) \tag{14}$$

where n is the wave group number computed as:

$$n(k) = 1/2\left(1 + \frac{2kh}{\sinh 2kh}\right) \tag{15}$$

After some algebra, the following equation in k is obtained:

$$\omega = \sigma(k)(1 - n(k)) \tag{16}$$

This equation can be solved numerically to obtain the abscissa k^* of the point of tangency and, then, the ordinate σ^* from the dispersion relation. Rearranging Equation (14) it is possible to compute the blocking velocity as:

$$|U| = \frac{\sigma^* - \omega}{k^*} \tag{17}$$

If a simple case is considered with constant water depth and velocity ($h = h(x)$ and $U = U(x)$), the dot product $\mathbf{U}\cdot\mathbf{k} = Uk$ gives ω as a constant values along rays (Eq. (9)). Further, the conservation of wave action (Eq. (11)) gives a constant wave action flux ($B = (U+C_g)\frac{1}{2}\frac{\rho g a^2}{\sigma} = const$). Moving towards blocking conditions, the factor $U + C_g$ goes to zero, thus leading to an increase of the wave amplitude a. This leads to a shortening and a steepening of incident waves while advancing on the adverse current, as also confirmed by the visual observations of Suastika (2004).

Similar experiments on the interaction between a shoaling wave and an opposing current are currently being conducted in the flume of the University of Parma by the research group led by Prof. Sandro Longo, within the activities of the "Mitigation and Adaptation in Resilient Coastal and estUarine integrated unitS - MARCUS" project. The flume is 10 m long, 0.30 m wide, and has a 1/74 slope designed to facilitate wave shoaling and the gradual reduction of current velocity as the water depth increases. The main experimental characteristics have been chosen to reproduce, through Froude scaling, the dynamics evolving at microtidal river mouths, with specific focus on the Misa River (see in the following). An example of a wave blocking condition is shown in Fig. 4. In this case, a regular wave train with $H = Xm$ and $T = Xs$, generated at a water depth $h = Xm$, encounters an opposing current induced by a constant flow rate of $Q = Xl/s$. This results in a mean velocity of $U = Xm/s$ at the blocking point. Fig. 4 also illustrates the wave deformation caused by the current. As waves propagate over the sloped bottom, they experience progressively stronger opposing currents in shallower waters. Consequently, the wavelength decreases, along with a reduction in wave height, due to shallow-water effects and nonlinear interactions.

Chen et al. (1998) improved the numerical modeling of wave current interaction trough an enhanced Boussinesq approach. Numerical simulations on the wave blocking of linear waves ($\epsilon < 0.023$) evolving from deep waters ($((h/L)_{short} = 0.53$) onto the intermediate waters of a bar ($(h/L)_{short} = 0.12$) were performed. Monochromatic short waves were blocked by an opposing current with velocity $|U| > C_g$ and their length decreased. The application of the analytical solution by wave action conservation was found to fail at wave blocking, prescribing a divergent amplitude. In addition, a frequency downshifting was observed over the blocking point. A potential longer wave mode ($(h/L)_{long} = 0.03$) over the bar superimposed on the previous short wave mode was not blocked by the opposing current. As a final effect, only longer waves (lower frequencies) could propagate beyond the blocking point, leading to a decrease in the dominant frequencies of the propagating waves past this point, thereby causing some frequency "downshifting".

3. Sea-river interactions at microtidal river mouths

By definition, microtidal environments are characterized by a tidal range (TR) of less than 2 m, distinguishing them from mesotidal (2 m $< TR <$ 4 m) and macrotidal ($TR >$ 4 m) systems (e.g. https://www.aviso.altimetry.fr/). Microtidal regimes dominate the majority of coastal areas worldwide, making them a prevalent feature of global river mouths (Fig. 5, adapted from https://www.aviso.altimetry.fr/). Studying microtidal systems simplifies the analysis by partially excluding tides as a major forcing factor. The three primary forces acting on river mouths—river discharge, sea waves, and tides—can be reduced to a dual interaction between river flow and waves, streamlining the interpretation of dynamics. Excluding funnel-shaped estuaries, characterized by linear sand ridges and where vertical stratification is influenced by flow reversal with significant tidal influences also narrows the scope to systems where river discharge and wave action dominate (Galloway, 1975). Microtidal river mouths can exhibit a wide range of morphodynamic behaviors depending on the relative influence of fluvial discharge and wave forcing. Traditionally, these systems have been classified according to the fluvial dominance ratio (r) defined as:

$$r = \frac{Q_r}{Q_{s,max}} \tag{18}$$

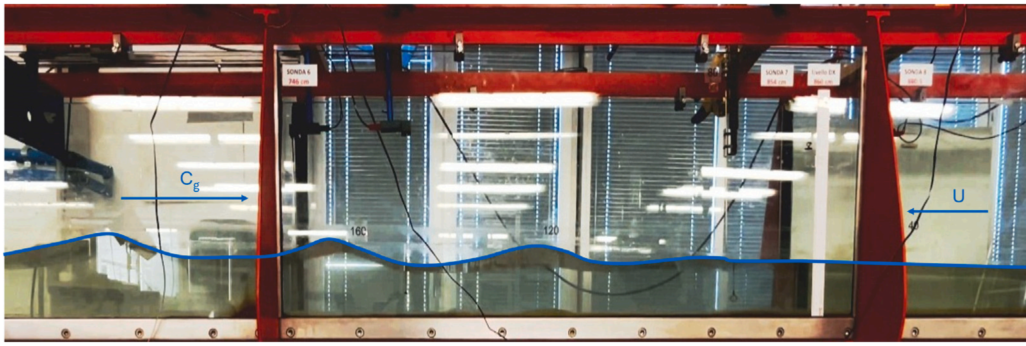

Fig. 4. A periodic incident wave train blocked by an adverse current as observed by Longo and his research group in the wave–current flume of the University of Parma.

where Q_r is the river sand flux and $Q_{s,max}$ is the maximum littoral sediment flux at the mouth (Nienhuis et al., 2015).

Values of $r > 1$ have been associated with fluvially influenced mouths, which generally exhibit prominent prodeltas shaped by sediment deposition from river outflows, while $r < 1$ typically describe wave-influenced ones, characterized by flattened profiles due to wave-driven sediment removal and redistribution alongshore.

However, the morphological outcomes of these settings are far more complex than a simple binary classification suggests. The r index provides only a first-order quantification of potential forcing balance and does not account for processes such as river-mouth sediment bypassing or the role of antecedent topography and inherited delta morphology. As discussed by Anthony (2015) and confirmed by recent numerical studies (e.g., Zăinescu et al. (2024)), wave and river processes interact through non-linear feedbacks that depend on sediment availability, deltaic geometry, and shoreline orientation. Strongly wave-influenced mouths do not necessarily develop flattened or alongshore-smoothed profiles. Many large deltas such as the Danube and the Rhône exhibit substantial wave reworking while retaining protruding delta lobes or spits shaped by long-term interactions between riverine sediment supply and wave redistribution (Zăinescu et al., 2021, 2024; Sabatier and Anthony, 2015; Boudet et al., 2017).

The core principles of our analysis are inherently applicable to wave–current interactions in general and allow to generalize the understandings to environments characterized by a limited tidal range. This broader applicability is supported by numerous examples drawn from the literature, which include both large-scale (Mississippi, Rhone, Pearl, Delaware) and small-scale (Maipo, Misa, Umgeni, Breede, Shoalhaven) microtidal rivers, represented, together with their tidal range, in Fig. 5. Moreover, Table 1 reports the main characteristics of each system. The interaction between river discharge and sea waves is critical in shaping both the average and extreme dynamics at microtidal mouths, as described in the following sections.

In particular, these examples have been used to reinforce our analyses and interpretations of the observed phenomena: (1) wave steepening and breaking at the Rhône and Misa rivers and wave refraction at the Mississippi and Misa rivers (Section 3.2.1); (2) upriver propagation of infragravity waves at the Maipo and Misa rivers (Section 3.2.2); (3) river plume deflection by waves at the Maipo and Misa rivers (Section 3.2.3); (4) mouth bar migration at the Rhône and Misa rivers (Section 3.3.1); and (5) compound flooding driven by wave–current interactions at the Breede and Misa rivers (Section 3.3.2).

The Misa River was selected as one of the test sites because it represents a real-world natural laboratory equipped with an integrated monitoring system that captures the interactions between river and marine forcings. This system includes a video-monitoring station, an X-band radar, a tide gauge, and several hydrometric sensors, providing high-resolution datasets that have been partly used in this manuscript. These observations have also supported previous numerical modeling

Fig. 5. Global map of tidal range showing the locations of the analyzed large-scale (red) and small-scale (yellow) rivers. Letters "R" and "W" indicate river-dominated and wave-dominated mouths, respectively.
Source: Adapted from Aviso+ https://www.aviso.altimetry.fr/.

studies investigating the wave–current interplay at the Misa River mouth, including its influence on plume dynamics and mouth-bar evolution (Baldoni et al., 2022, 2021). Results presented in Sections 3.2.3 and 3.3.1 derive from those earlier modeling efforts, whereas Sections 3.2.1 and 3.3.2 introduce new applications developed within the present study. All the analyses were performed with the Delft3D numerical suite, dynamically coupling the modules responsible for the simulation of water circulation driven by tides, waves, and river inflow (FLOW), and wave propagation and transformation (WAVE) (Deltares, 2025a,b). The domain discretization was identical for all applications except for the preliminary compound-flooding analysis presented in Section 3.3.2, for which the Flexible Mesh version of Delft3D was employed (Deltares, 2025c).

Two grids were nested for WAVE computations. The larger grid extended up to a depth of 10 m, with 30 m resolution; the smaller grid had a variable resolution, ranging from 8 m offshore to 3 m inside the river. For the FLOW model, two grids were connected through the domain decomposition approach. The outer grid was obtained by reducing the

Table 1
Characteristics of the microtidal estuaries shown in Fig. 5: main river, basin area, mean annual discharge (Q), tidal range, mean annual wave height (H_s) and storm surge. References are shown in the first column. Data for the Misa River derived from observations. Values of H_s at a water depth d were retrieved from the Copernicus dataset "Global Ocean Waves Reanalysis": https://doi.org/10.48670/moi-00022.

Main river	Basin area km^2	Q m$^3/s$	Tidal range m	H_s m	Storm surge m
Misa (IT)	383	4	0.6 (max)	0.39 (d=12)	0.8
Rhône (FR) (Sabatier et al., 2009)	96 500	1710	0.3 (mean)	0.54 (d=11)	1
Mississippi (USA) (Mikhailov and Mikhailova, 2010; Levin, 1993)	3 238 000	16 790	0.35 (mean)	0.73 (d=10)	3–5
Maipo (Chile) (Roco et al., 2024; Flores et al., 2022; Winckler et al., 2017)	15 000	30	1.5 (max)	1.32 (d=44)	2
Breede (ZA) (James et al., 2018; Kupfer et al., 2022; Rautenbach et al., 2020)	12 600	56	2 (max)	2.15 (d=35)	0.9
Umgeni (ZA) (Gerritsen et al., 2019; Cooper, 2002; Rautenbach et al., 2020)	4439	21	2 (max)	1.58 (d=35)	0.6–0.9
Shoalhaven (AUS) (Kumbier et al., 2018; Ji et al., 2025)	7150	27	1.5 (max)	0.96 (d=23)	0.85
Pearl (CN) (Li et al., 2023; Yuxing et al., 2020)	353 100	10 000	1.4 (mean)	0.25 (d=17)	1–2
Delaware (USA) (McKeon and Piecuch, 2025; Xiao et al., 2021)	37 568	330	1.5 (mean)	0.4 (d=9)	0.6–1.8

WAVE larger grid by some cell lines at the boundaries, while the inner grid coincides with the WAVE smaller grid. For the compound flooding model (Section 3.3.2), the WAVE domain was discretized with two nested grids with 15 m and 5 m resolution, covering depths up to 10 m. The FLOW grid was instead characterized by unstructured meshes, with a resolution ranging from 50 m in the offshore and inland regions not interested by flooding, to 2.5 m inside the river.

For all the applications, timeseries of wave parameters (H_s, T_p and direction) were used to force the WAVE module, while the FLOW boundary conditions included: (i) a total-discharge time series applied at the river boundary; (ii) a water-level forcing at the offshore boundary; and (iii) a Neumann-type condition at the cross-shore boundaries. For the plume analysis, an additional input concentration was also prescribed at the river boundary.

For morphodynamic simulations (e.g.; those for the mouth bar and plume analyses), the riverbed was characterized by a mixture of sediment ranging from 100% cohesive material at the upriver section, to 100% sand just outside of the river mouth, accordingly to the observed site characteristics. A small amount of gravel was also considered at the mouth bar location. Sand and gravel were characterized by a median diameter of 0.18 mm and 6 mm, respectively, while cohesive material was described through (i) critical shear stresses for erosion and sedimentation of $0.3\mathrm{N/m^2}$ and $0.4\mathrm{N/m^2}$, respectively, (ii) erosion parameter of $1\mathrm{e}{-04}\ \mathrm{kg/m^2/s}$ and (iii) settling velocity of $0.1\mathrm{mm/s}$. The Manning coefficient was set to $0.015\text{-}0.02\mathrm{m^{1/3}/s}$ and $0.07\mathrm{m^{1/3}/s}$ in the wet and dry areas, respectively. Models were calibrated and validated in terms of water levels, depth-averaged velocity and wave propagation with data from the monitoring system and offshore buoys. For further details, the reader is referred to Baldoni et al. (2022, 2021).

The processes influencing the dynamics at the river mouths exhibit varying levels of energy and complexity. These dynamics can be broadly classed into two main types: the average or baseline dynamics, which represent the typical behavior of the key phenomena and their interactions under normal conditions, and the more energetic and intense dynamics associated with extreme events, such as floods, storm surges, or high-energy wave activity, as well as a combination of more of them. Understanding both the average and extreme dynamics is crucial to comprehensively analyze the interplay of hydrodynamic, sediment transport, and morphological processes in these highly dynamic environments. The average dynamics can be influenced by short- and long-wave propagation, river plumes and wave refraction. Among the high energy processes, particular attention must be given to the inlet morphology with the associated formation, migration and expulsion of mouth bars into the sea, and the effects of compound flooding. Field observations of the main phenomena occurring at river mouths are presented in the following sections.

Although our analysis focuses on the cross-shore interactions between riverine and wave-induced flows, a brief description of longshore processes is also given, since they play a key role in shaping the morphology of river mouths.

3.1. The longshore component of river mouth morphodynamics

Alongshore processes controls not only the local balance between fluvial and marine sediment fluxes, but also governs key morphological outcomes such as mouth migration, sediment bypassing, and the development of mouth-attached spits (Anthony, 2015; Sabatier and Anthony, 2015). These processes are particularly relevant for coastal stability along adjacent shorelines, as sediment exchanges across river mouths can either nourish or starve neighboring coasts.

The interplay between river discharge and longshore currents creates a highly dynamic and non-linear system. At energetic river mouths, strong riverine outflows can locally suppress or redirect longshore transport, while during low-flow conditions, wave-induced currents tend to dominate, promoting the alongshore redistribution of sediments (Zăinescu et al., 2021; Boudet et al., 2017). Morphological feedbacks associated with mouth bar dynamics further complicate this picture, often leading to alternating phases of mouth closure and opening, or to the formation of large spits extending downdrift from the mouth, as observed in several deltaic systems such as the Rhône (Sabatier and Anthony, 2015; Boudet et al., 2017), the Danube (Zăinescu et al., 2021, 2024) and the Ebro (Jiménez et al., 1997).

The conceptual and numerical modeling of river–wave interactions at river mouths has increasingly emphasized the critical role of the longshore component in shaping morphodynamic outcomes. Longshore currents, generated by obliquely incident waves, act as an efficient mechanism for sediment redistribution, controlling sediment bypassing across river mouths and the development of mouth-attached spits (Sabatier and Anthony, 2015; Boudet et al., 2017). These currents interact dynamically with river outflows, producing alternating dominance patterns in which either river jets or wave-driven longshore transport prevail (Zăinescu et al., 2021). Such interactions determine whether sediment is trapped near the mouth, bypassed downdrift, or reworked into mouth bar and spit systems, thus exerting first-order control on the stability and morphology of the river mouth zone (Anthony, 2015).

Numerical experiments and field observations in the Rhône and Danube deltas (Boudet et al., 2017; Zăinescu et al., 2024) have shown that the efficiency of sediment bypassing and long-term morphological evolution depend on the relative magnitude of riverine versus wave-induced sediment transport. When longshore fluxes exceed fluvial export, sediment tends to accumulate downdrift, fostering spit elongation and partial mouth closure; conversely, during periods of high river discharge, jet expansion can temporarily interrupt longshore transport and promote seaward sediment export. This shifting dominance highlights the inherently non-linear character of wave–river coupling.

Despite significant advances in process-based modeling (e.g., Delft3D), the representation of longshore sediment dynamics remains limited by the difficulty of resolving wave–current feedbacks, surf-zone turbulence, and rapidly changing mouth geometries (Dodet, 2013; van der Westhuysen, 2012). The recent work by Zăinescu et al. (2024) demonstrates that even with reduced complexity, numerical models can reproduce realistic patterns of longshore current balances and sediment bypassing, yielding morphologies consistent with field observations. However, given the strong spatio-temporal variability and morphological feedbacks involved, conceptual and empirical approaches (Anthony, 2015) continue to provide essential frameworks for interpreting longshore-driven morphodynamics at river mouths.

3.2. Average dynamics

3.2.1. Short-wave evolution

The interaction of waves with opposing currents at river mouths results in increased wave amplitude, wave blocking, and, ultimately, wave breaking. A portion of the wave energy is reflected seaward, while the direction of wave propagation is altered due to refraction. The following examples demonstrate how these processes coexist at river mouths, along with the evolution of wave refraction.

River-sea interaction can produce striking wave phenomena, as observed at locations such as the Umgeni River mouth in Durban, South Africa. Here, the fronts of incoming sea waves often adopt a characteristic V shape due to the interaction with the river outflow (see www.youtube.com/watch?v=PkEfhRii-AI). This setting provides a clear example of wave blocking, where opposing currents reduce the group velocity of incoming waves, potentially halting their progression. Additionally, wave reflection is noticeable, as part of the wave energy is directed back towards the sea, while wave refraction, driven by varying current velocities across the river mouth, manifests itself as a change in wave direction. These processes interact dynamically, creating a unique environment where the interplay between river outflow and sea waves can be distinctly observed.

Wave blocking and breaking phenomena at the mouth of the Rhône River have been investigated by Sabatier et al. (2009), highlighting the role of river discharge in modulating coastal wave dynamics. Two scenarios were compared: the first (case 1) representing the simultaneous occurrence of a 1-year return period river discharge and storm waves (H_s = 3 m, T_p = 7.5 s and Q = 3000 m^3/s); and the latter (case 2), featuring the same storm waves but with no river discharge (H_s = 3 m, T_p = 7.5 s and Q = 0 m^3/s). They used the Numerical Model for simulating Longshore current-Current–Wave interaction (NMLong-CW model) to compute the longshore sediment transport (LST) given a specific bathymetric profile, the wave characteristics and the river discharge.

The results of the model in terms of wave height and LST for the two cases are reproduced in Fig. 6a and the bathymetric profile is plotted in Fig. 6b. The presence of the river current in case 1 was found to significantly attenuate wave energy, reducing the offshore significant wave height from 2.6 m to 2.1 m. Consequently, the LST rate also decreased from 0.07 $m^3/m/s$ to 0.05 $m^3/m/s$ when river flow blocks the waves in the mouth sector. Notably, due to the high wave nonlinearity ($\epsilon \approx 0.7$), the interaction between the river outflow and the incoming waves led to wave breaking rather than reflection, emphasizing the dominant role of nonlinear processes in such river-mouth environments.

Similar interactions occur at small-scale rivers, such as the Misa River in Senigallia, Italy, which serves as a test site for the "Mitigation and Adaptation in Resilient Coastal and estUarine integrated unitS - MARCUS" project and is here used as reference for a number of

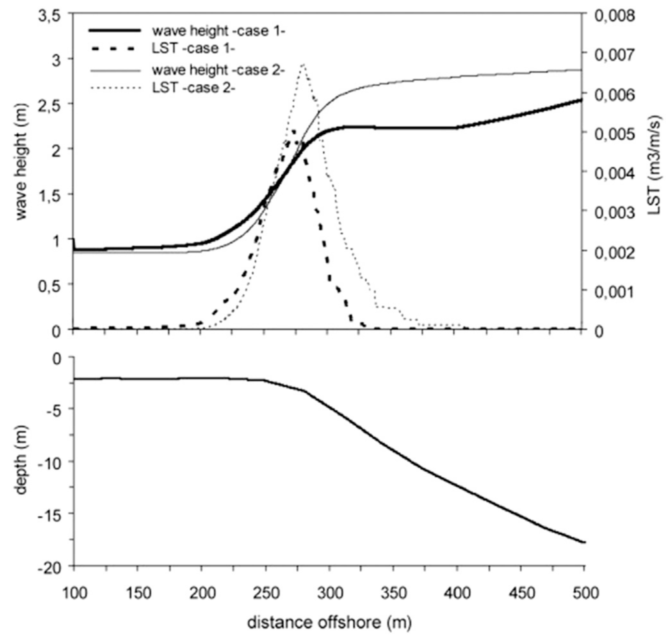

Fig. 6. Panel a: Wave height and LST for the two cases. Panel b: Bathymetric profile. Reprinted from Connecting large-scale coastal behavior with coastal management of the Rhône delta, 2009, Vol. 107 (1-2), Sabatier F., Samat O., Ullmann A. and Suanez S., Geomorphology, Pages 79–89.
© 2008 with permission from Elsevier.

analyses. Footage from the SGS videomonitoring station (www.morse.univpm.it), included in the Supplementary Content (Video 1), clearly illustrates the complex wave dynamics at this location. Here, the interaction between river outflow and incoming waves results in noticeable wave refraction, as the waves bend and change direction due to the varying current patterns. In addition to refraction, wave steepening and breaking can be observed as the incoming waves encounter the opposing river current, causing the waves to become steeper and eventually break. These processes, in combination, highlight the dynamic and ever-changing conditions at the river mouth. To further investigate this behavior, Delft3D numerical simulations were performed for the Senigallia test site. Simulations were run under two scenarios: one with waves alone (W) and another one forced with both waves and an opposing river discharge (W+Q). Wave characteristics from a real storm that occurred in the area were used (H_s = 5.22 m, T_p = 8.39 s, and θ = 20° N, where θ indicates the wave direction). A moderate river discharge of 100 m^3/s was also considered in the waves on opposing current (W+Q) test. Simulations results confirmed the observed wave dynamics. The increase in wave steepening is shown in Fig. 7.

In the left panel, the wave steepness for the wave-only test is displayed, while the right panel shows the steepness for the waves combined with the river current. Although the numerical model used for this simulation is not ideally suited to highlight such phenomena due to its phase-averaged nature, a remarkable increase in wave steepness is observed at the river mouth and waves are able to propagate inside the river for a shorter distance. When the opposing current is present, the wave steepness doubles compared to the wave-only case. This is due to the simultaneous reduction in wavelength and increase in wave amplitude. In addition, Fig. 8 confirms intense wave breaking by inspecting wave dissipation. The area where the majority of wave dissipation occurs corresponds to the visual observations obtained from the SGS monitoring system (Video 1 in Supplementary Content).

Another phenomenon observed as a result of the numerical simulation is wave refraction. Its effect is represented by the difference in the mean Cartesian direction of propagation between the wave-only

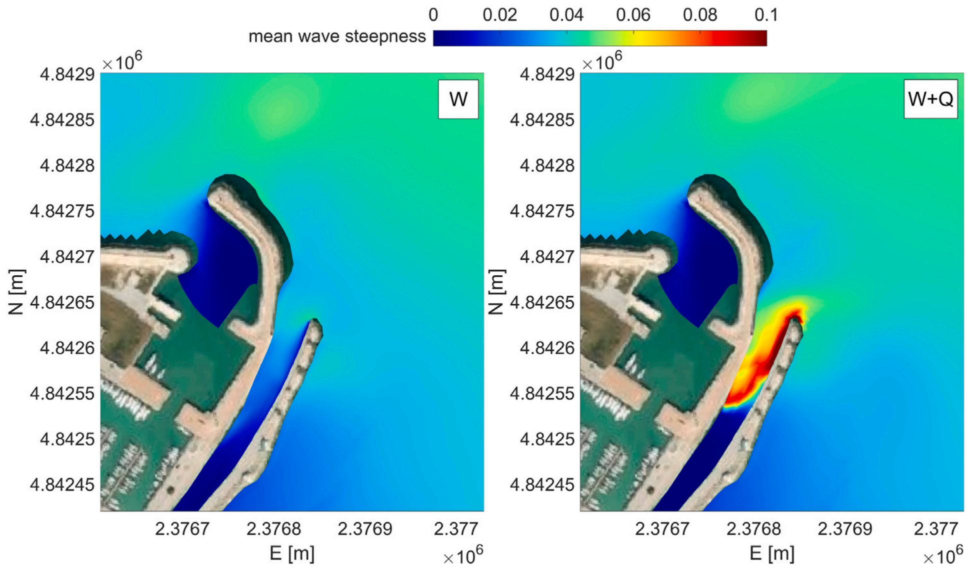

Fig. 7. Wave steepness at the Misa River mouth. Left panel: wave only (W). Right panel: wave and opposing current (W+Q).

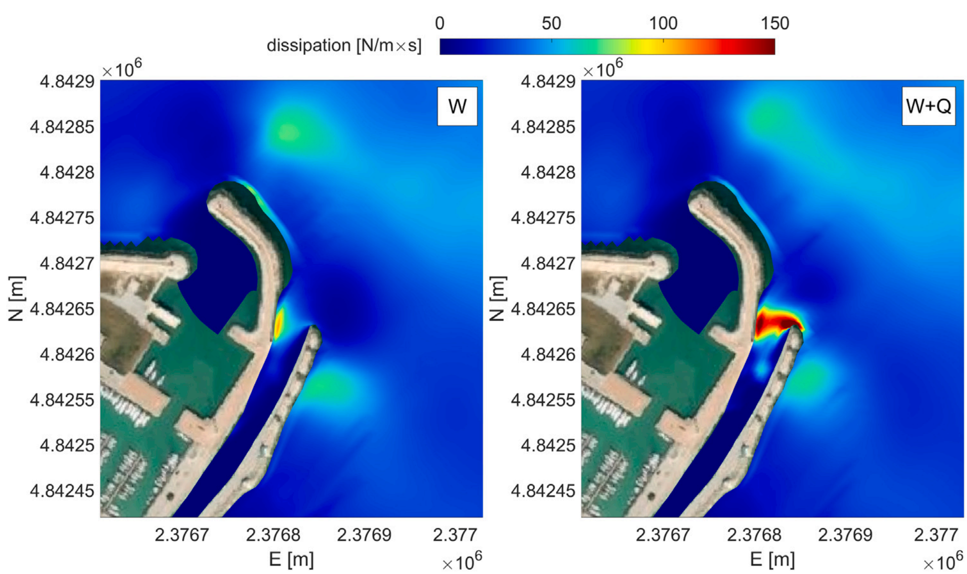

Fig. 8. Wave dissipation at the Misa River mouth. Left panel: wave only (W). Right panel: wave and opposing current (W+Q).

test and the test with opposing current, as shown in Fig. 9. Positive values indicate a counter-clockwise rotation of the velocity vectors when an opposing current is present, while negative values correspond to a clockwise rotation. The result of this current-induced refraction is that the wave vectors tend to be directed more towards the center of the river mouth. This effect is due to the term $k_j \frac{\partial U_j}{\partial x_i}$ in Eq. (9).

A similar behavior is observed in large-scale systems, such as the case of the Mississippi River. Sorourian et al. (2020) used the fully-coupled FVCOM-SWAVE model to investigate wave–current interactions. They found that waves on the shelf side of the inlets are influenced by the gyre currents induced in the Louisiana Bight, which lead to wave refraction. These currents include the Mississippi River plume, alongshore current, and tidal jet in the Barataria Pass. The FVCOM-SWAVE model predicts a reduction in significant wave height inside the Louisiana Bight, attributed to current-induced refraction and the wave-stretching effect caused by the clockwise gyre from the Mississippi plume. The wave dynamics at the mouth of Barataria Pass are influenced by both the intensity of the jet velocity and the local wind direction, resulting in wave steepening and partial wave blocking when the current is opposing, and a reduction in wave height when the current is following. During ebb flow, the opposing current can increase wave height by approximately 20%, while the following current can lead to a decrease in wave height of up to 15% on the seaward side of Barataria Pass.

3.2.2. *Long-wave upriver propagation*

Long waves, usually in the form of Infragravity Waves (IGW), are characterized by wave periods in the range ≈ 25 − 250 s. In tidal estuaries they have been widely observed (Uncles et al., 2014; Bertin and Olabarrieta, 2016). The tide is dominating the process so much that no upriver propagation is observed during ebb stages. However, observations of IGW upriver propagation in microtidal systems are becoming more frequent. In such environments, the tide only modulates the upriver propagation of IGW, which is mostly favored by storm surge. Some examples are here reported to highlight the filtering of high-frequency modes by wave blocking and breaking, with a consequent frequency downshifting.

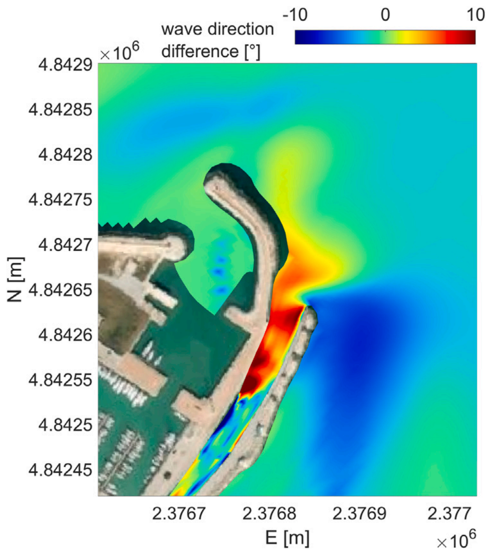

Fig. 9. Difference in wave direction between the wave only (W) and the wave with opposing current (W+Q) tests at the Misa River mouth.

For the Misa River, IGW are found to travel upriver during a storm, with celerity in the range $(3.6 - 5.5)$ m/s, which is typical of nonlinear long waves. The propagation can extend up to about 15 times the swell length and get enhanced by tide-induced increase in water depths (Melito et al., 2020). Fig. 10 shows the wave energy upriver propagation during a sea storm event. The total wave energy strongly dissipates due to wave breaking before entering the river mouth, as shown in panel a. Swell waves (panel b) follow a similar behavior, the combined action of depth-induced wave breaking and opposing river current enhanced by rainfall drastically reduces short wave energy. On the contrary, IGW propagated upstream (panel c). The percentage of energy related to long waves with respect to the maximum offshore total wave energy increases moving upriver, showing an overall frequency downshifting. Such upriver propagation of IGWs is typically associated with large flood tidal stages. Therefore it is especially noteworthy given the negligible tidal excursion in the area due to the fact that such propagation.

Flores et al. (2022) investigated the interaction between IGW and the plume dynamics of the Maipo River, a small river discharging into a high-energy surf zone along the Chilean coast. Their study found that the plume exiting the river mouth is deflected alongshore by wave action. Using cross-shore timestack analysis, the surf zone edge and the plume edge were identified, along with their oscillatory motion corresponding to the frequency of IGW. ADCP measurements revealed that a significant portion of the spectral energy at the plume edge resides in the infragravity band. The inlet dynamics, including plume behavior and surf zone width, were found to be strongly influenced by IGW. This modulation appears to result directly from a time-varying breakpoint, which drives both surf zone and river mouth dynamics.

3.2.3. River plume and wave refraction

River plumes are largely governed by river discharge (Q) and wind stress. However, significant is also the role of waves and tides, which enter the river mouth and can stir the riverbed sediment putting in suspension large quantities of fine sediment. At microtidal rivers this action is largely due to sea waves, which are seen to provide a significant bed shear stress also for weak river discharges.

The monitoring system at the Misa River mouth provided valuable insights into the role of waves in influencing river plumes. Videomonitoring observations revealed the formation of plumes even in the absence of significant river discharge events. Starting with the plume tracking from images, Baldoni et al. (2022) studied the Misa River plume evolution, focusing on its generation and transport mechanisms. The combination of observations with information derived from numerical modeling allowed to better assess the effect of different forcing. Several Delft3D morphodynamical simulations were run, activating alternatively the river discharge or the wave forcing, with different intensities. The riverbed was mainly characterized by cohesive sediments, with critical shear stress for erosion equal to $0.3\mathrm{N/m^2}$. Apart from the main role of the river flow in the generation and consequent offshore expansion of the plume, wave activity was found to increase bed shear stress within the river mouth, reaching the critical threshold for bed erosion and sediment suspension, which ultimately leads to plume generation. Moreover, as wave intensity increases, wave-driven alongshore currents become stronger, pushing the plume alongshore and significantly reducing its offshore extent. Fig. 11, adapted from Baldoni et al. (2022), shows the plume front generated by four different wave conditions (H_s = 2 m and 4 m for two wave directions, 90°N and 20°N). The plume is defined as the area where the sediment concentration exceeds a reference concentration typical for the Adriatic Sea (0.05 $\mathrm{kg/m^3}$). Results shown in Fig. 11 confirm that waves are responsible of 1) stirring sediments at the river mouth, generating plumes (as observed from the videomonitoring products) and 2) moving the plume alongshore as the wave-driven currents intensify.

Roco et al. (2024) used in-situ observations collected at the Maipo River mouth to examine the interplay between river outflow and incident wave forcing, which affects the distribution of freshwater along the coastline. Their findings revealed that wave–current interactions cause wave fronts to bend and refract in response to the opposing river outflow, particularly during the late ebb phase (left panel in Fig. 12). As waves propagate shoreward and interact with the plume jet, the wave fronts undergo refraction and steepening.

The right panel of Fig. 12 presents a schematic illustration of wave front propagation against a plume, which is characterized by a maximum velocity U_2 along the jet's centerline. At a specific longshore distance, another reference line (denoted by subscript 1) can be identified where the plume's influence is negligible, such that $U_1 = 0$ m/s. At the centerline, the wave celerity changes due to the opposing currents ($C_{\omega 2} = C_{\sigma 2} - U_2$). Wave fronts bend and refract due to the opposing river outflow. For wave fronts normal to the wave current direction, the wavelength at a certain location L_j can be computed by numerically solving the following Equation (Jonsson and Skovgaard, 1978):

$$\sqrt{\frac{h}{L_2}\tanh\frac{2\pi}{L_2}h} = \sqrt{\frac{h}{L_0}}\left(1 + \frac{U_2 T}{L_1}\right) \tag{19}$$

As a consequence, at location 2, where $U_2 > U_1 = 0$, the wavelength L_2 is smaller than the undisturbed wavelength (L_1) at the same water depth.

3.3. Extreme dynamics

3.3.1. Inlet morphology and mouth bar dynamics

Microtidal rivers can transport significant amounts of sediments, which contribute to the formation of bend bars and mouth bars. In the absence of waves, a mouth bar typically forms just seaward of the river mouth, at a distance approximately twice the river width. This process is driven by the expansion of the river jet into the sea, leading to a reduction in flow velocity and enhanced sediment deposition (Fagherazzi et al., 2015).

The dynamics of mouth bars, however, can be strongly influenced by the action of waves and longshore processes, especially in wave-influenced deltas, where bars can be eroded or migrate alongshore, with sedimentation patterns depending on the river–wave energy balance (Zăinescu et al., 2024). Littoral transport, driven by wave-induced currents, interacts with river outflows and shapes coastal morphology (Anthony, 2015). High and oblique incident waves enhance longshore circulation and promote sediment bypass from river mouths to

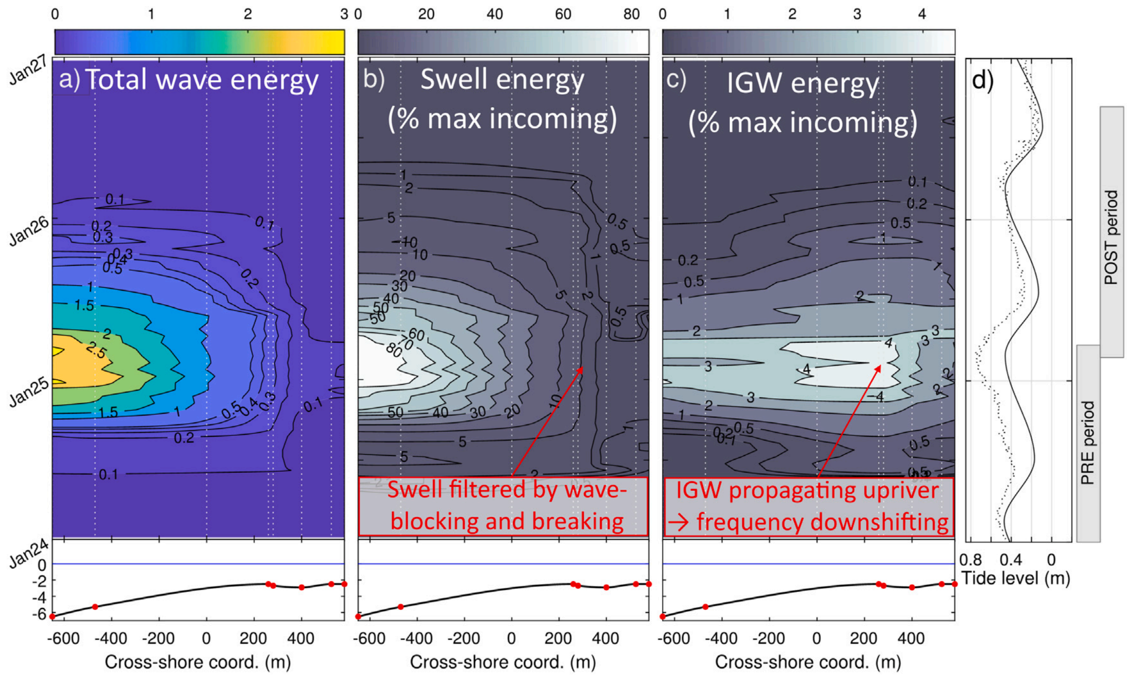

Fig. 10. Total wave energy (panel a), percentage of swell wave energy (panel b) and of IG wave energy (panel c) relative to the maximum incoming. In panel d, the comparison between the astronomical tide at Ancona (black line) with the tidal level measured at Ancona harbor (dotted line) is reported.
Source: Adapted from Hydrodynamics at a microtidal inlet: Analysis of propagation of the main wave components, 2020, Vol. 235 (106603), Melito L., Postacchini M., Sheremet A., Calantoni J., Zitti G., Darvini G., Penna P. and Brocchini, M., Estuarine, Coastal and Shelf Science.
© 2020 with permission from Elsevier.

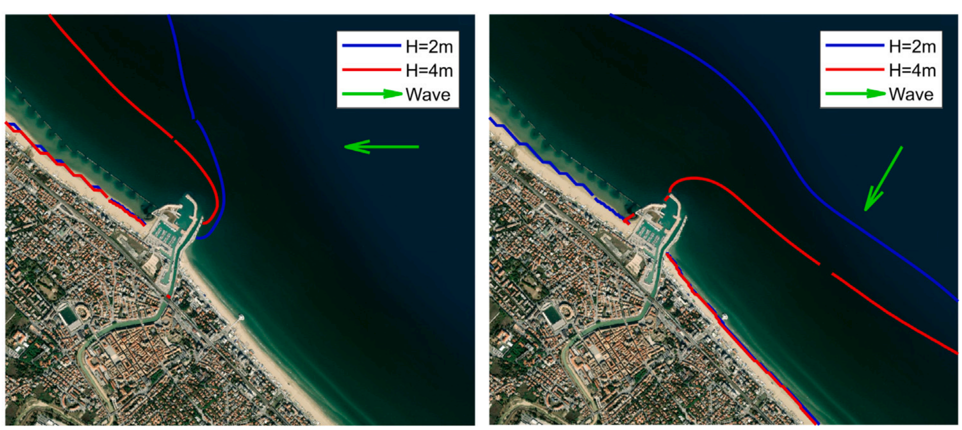

Fig. 11. Plume edge associated to different wave heights and directions. Blue and red lines identify the plume edge for simulations forced with 2 m and 4 m wave height (at 12 m water depth), respectively. Green arrows show the wave incoming direction, $90^{\circ}N$ (left panel) and $20^{\circ}N$ (right panel).
Source: Adapted from A comprehensive study of the river plume in a microtidal setting, 2022, Vol. 275 (107995), Baldoni A., Perugini E., Penna P., Parlagreco L. and Brocchini, M., Estuarine, Coastal and Shelf Science.
© 2022 with permission from Elsevier.

adjacent coasts, while low waves approaching normal to the shoreline tend to generate diverging longshore currents over the mouth bar crest, interrupting the longshore circulation (Zăinescu et al., 2021). Intense river discharge dissipates wave energy via blocking and refraction, disrupting wave-induced longshore currents. The resulting hydraulic groyne effect favors bedload stabilization and accumulation, promoting river-mouth bar formation (Anthony, 2015).

In the small-scale system of the Misa River, river currents are found to dominate over wave-induced processes (Baldoni et al., 2021). The Misa River, characterized by a torrential flow regime, can transport substantial sediment loads, with peak discharges of approximately $800\text{m}^3/\text{s}$ during 100-year return period flood events. The mouth bar dynamics was, first, studied through observations from the monitoring system operating at the Misa River estuary and, then, simulated using the Delft3D modeling suite. Simulations were forced only by river discharge, only by waves and by their combination, reproducing an observed event. The riverbed composition was mainly characterized by cohesive material, with the percentage of fine sand increasing in the last 300 m of the river. Both observations and modeling show that the evolution of the mouth bar is predominantly controlled by the river discharge. A relatively frequent discharge, such as that associated with a 1-year return period, can induce a downriver bar migration of 50–100 m, typically resulting in the expulsion of the bar out of the river mouth. On the other hand, strong wave events, corresponding to a 10-year return period, can result in a smaller and slower upriver migration of 25–30 m, comparable with the Misa River cross section width. The

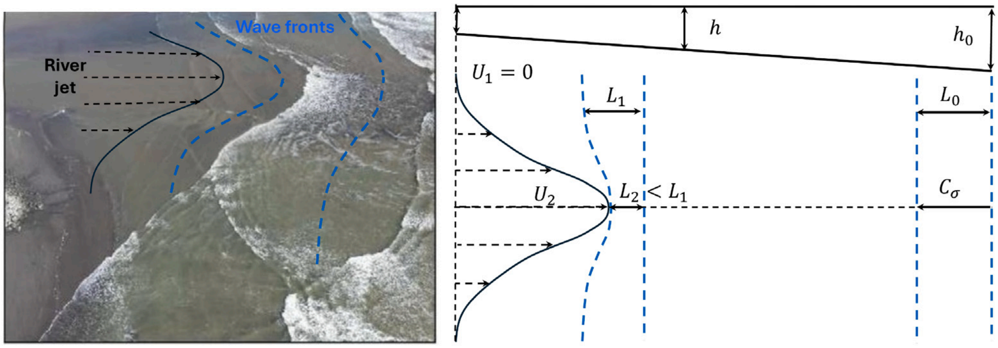

Fig. 12. The left panel shows the refracted wave fronts due to the interaction with an opposing current adapted from Roco et al. (2024). The right panel shows a sketch of wave refraction due to wave–current interaction.

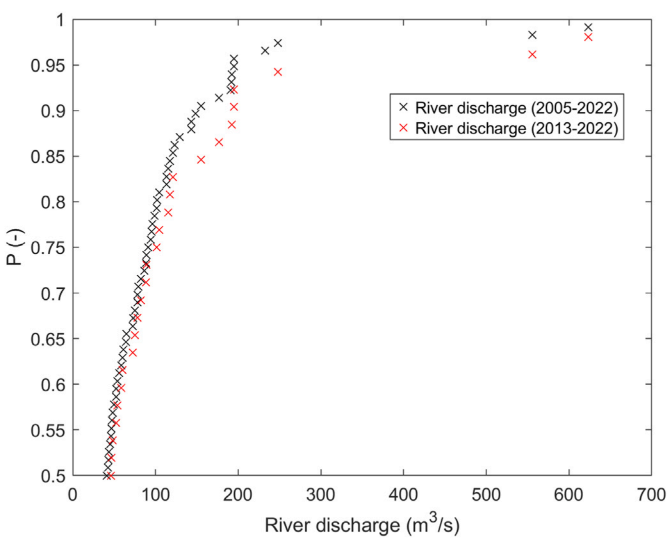

Fig. 13. Non-exceedance probability of the river discharges in the Misa River for the periods 2005–2022 (black) and 2013–2022 (red).

real-case event shows that, even when the river current acts simultaneously with waves, its influence dominates, eroding the bar and pushing sediments seaward. These contrasting behaviors highlight the complex interplay between riverine and marine processes in shaping mouth bar dynamics. Frequent river discharges exert sustained control over sediment transport and deposition, causing the mouth bar to migrate seaward as sediment is progressively delivered to the coastal zone. On the other hand, rare but energetic wave events disrupt this process by eroding the mouth bar and redistributing sediments landward via wave-induced turbulence and currents.

A support to the above dynamics comes from recent hydrological trends observed at the Misa River. An analysis of the river discharges recorded at the Misa gauging station was performed over two different periods: the entire observation record (2005–2022) and its second half only (2013–2022). Results shown in Fig. 13 reveal that for discharges below $100 m^3/s$, the trend remains substantially unchanged between the two datasets. Above this threshold, however, the curves diverge. In particular, the dataset corresponding to the second period associates, for each discharge value, a lower non-exceedance probability (P). This indicates that the likelihood of exceeding the same discharge value is higher when the analysis is limited to the most recent part of the dataset. This pattern, characterized by extended periods of low flow during which the mouth bar can migrate upriver, interrupted by few but intense floods capable of flushing the bar out of the mouth, amplifies the mechanisms connected to the cyclic mouth-bar evolution.

A similar behavior is observed at the mouth of the Rhone River, where Grain-Size Trend Analysis (GSTA) has been employed to investigate sediment-transport mechanisms (Maillet et al., 2011). During weak flood events, characterized by low river discharge, sediment transport is primarily confined to the inner part of the river mouth, coinciding with the location of the mouth bar. However, during extreme flood events, such as those with a 50-year return period, the river's influence extends to the eastern part of the mouth, and the mouth bar is expelled further seaward. This observation underscores the critical role of flood magnitude in controlling sediment transport pathways and mouth bar dynamics. Under low-discharge conditions, sediment deposition remains localized, facilitating mouth bar stabilization and growth. In contrast, extreme flood events significantly increase the river's sediment-carrying capacity, enhancing sediment dispersion across a broader area and forcing the mouth bar to migrate outward.

3.3.2. Compound flooding of river mouth areas

Flooding events in coastal and estuarine areas result from complex interactions between multiple physical drivers. Among these, compound flooding has gained increasing attention in recent years due to its potential to exacerbate extreme water levels and increase flood risk. Unlike traditional approaches that analyze individual drivers in isolation, compound flooding considers the interplay between different hydrodynamic processes, particularly at the interface of riverine and coastal systems.

In this study, we focus on the physical aspects of surface flows to enhance the understanding of compound flooding dynamics. Our analysis deliberately excludes atmospheric forcing mechanisms such as atmospheric rivers, which are known to contribute to extreme precipitation but fall beyond the scope of this work. Similarly, we do not address hyporheic flows or bio-ecological processes, as our emphasis remains on hydrodynamic interactions rather than subsurface or ecological components. As anticipated in the Introduction, a key aspect of our investigation is the river-sea interaction, which plays a crucial role in modulating flood conditions in estuarine and deltaic environments. The combined effects of river discharge and sea levels can create highly nonlinear responses, leading to extreme water levels that are difficult to predict using conventional flood assessment methods. Understanding these interactions is essential for improving flood hazard assessments and developing more effective mitigation strategies, particularly in the context of climate change and sea level rise.

Kupfer et al. (2022) investigated compound flooding from tides, river discharge (Q), and waves (W) using Delft3D model at the Breede Estuary, in South Africa. No storm surge contribution was considered because it is assumed to be relatively small compared to other flood drivers in most South African estuaries. The comparison between compound (STWQ), waves-only (STW), and discharge-only (STQ) scenarios highlights key differences in flood extent and controlling mechanisms. Results indicate that the flood extent is primarily controlled by river discharge (Q) rather than waves (W). Specifically, Q exerts the greatest influence in the upstream section, while W play a dominant role in the mouth area. Flooding at the river mouth is largely driven by wave setup, which results from wave–current-induced breaking.

A similar approach was applied to the Misa River, Italy. A numerical model based on Delft3D-FM was used to simulate compound flooding driven by river discharge, tide, storm surge, waves, and sea level rise (SLR). In the present study, a parametric approach was employed to evaluate the impact of the primary flood drivers, river discharge and storm surge. This represents a preliminary phase of the work; a more detailed analysis, currently in progress, will rely on the statistical occurrence of the main forcings of compound flooding.

An unstructured grid, extended 3 km in both alongshore and cross-shore directions, was built to run the FLOW module. The resolution varies from a maximum of 50 m, offshore and in marginal areas not affected by flooding, to a minimum of 2.5 m inside the river. For the wave propagation, two structured grids were nested: the outer one, with resolution of 15 m, extends up to 10 m water depth; the inner one, with 5 m resolution, stretches as far as 6 m water depth. The FLOW and WAVE modules were online coupled to let them interact in a dynamic way. The bathymetry was created combining multiple sources of information, always prioritizing the most resolved dataset: a survey of the final river stretch and estuarine area of March 2024 (0.1 m), a digital terrain model (DTM) of the Misa River basin of May 2024 (0.5 m), a survey of the coastal area of Senigallia of 2022 (2 m), EMODnet bathymetry for the offshore region (~80 m). Four different hydrodynamic simulations were performed to assess the flood extent under a combination of factors. The duration of each simulation was 2 days. The choice of forcing factors is parametric; therefore, even though they represent plausible extreme values for the study site under the effect of climate change, their combination is not derived from specific statistical analyses. For the choice of the intensity of each factor we relied on climate change adaptation studies already performed in the Marche Region (Baldoni et al., 2025, 2024), where the forcing were projected to 2070 under a SSP5-8.5 scenario (Arias et al., 2021). The focus of the present preliminary study is on the relative role of river discharge and storm surge, the latter here considered as the main contributor to the sea superelevation. Therefore, in this phase, wave characteristics and SLR were kept constant across the different tests. A scenario without tide was also simulated to verify the marginal influence of such forcing in a microtidal environment. The WAVE model was forced at the offshore boundary with a triangular timeseries of JONSWAP spectra, with the peak, occurring after one day, characterized by $H_s = 5$ m, $T_p = 9$ s and $dir = 30° N$, values that can be associated with a 20-year return period (Baldoni et al., 2025). According to previous studies conducted in the area (Baldoni et al., 2025, 2024), SLR due to climate change was projected to 2070 under the SSP5-8.5 scenario of the IPCC 6th Assessment Report (Arias et al., 2021). The corresponding SLR value, obtained from the NASA Sea Level Projection Tool (https://sealevel.nasa.gov/ipcc-ar6-sea-level-projection-tool), is 0.36 m. For the FLOW model, a constant water superelevation, equal to the sum of SLR and storm surge, was superimposed to a sinusoidal tidal timeseries with a 0.3 m amplitude. Such tide represents an extreme condition at the Misa River estuary, where the tidal range rarely exceeds 0.6 m. To evaluate the effect of an extreme storm surge, two values were chosen: 1 m, corresponding to a 20-year return period, and 1.5 m, associated with a return period exceeding 200 years (Baldoni et al., 2025). Moreover, a triangular discharge timeseries was imposed at the model river section. Peaks of river discharge were chosen as values occurring on average once a year at the Misa River. This choice was made to limit the dominance of such factor on the flooding: the selection of extreme discharges would have led to flooding almost entirely determined by the river overflowing, making it difficult to distinguish the role of varying sea level. The characteristics (maximum values of the forcing) of the simulations are summarized in Table 2. The Manning coefficient varied from 0.020 s/m$^{1/3}$ to 0.070s/m$^{1/3}$, respectively for sandy/riverbed and urbanized areas. The resulting flood extent is illustrated in Fig. 14, where the flooded area is colored according to water depth in each computational cell.

Table 2
Test characteristics for compound flooding simulations.

ID	Q (m^3/s)	Tide (m)	Surge (m)	SLR (m)	H_s (m)	T_p (s)	*Dir* (°N)
1	150	0.3	1.0	0.36	5.0	9.0	30.0
2	150	0.3	1.5				
3	150	0.0	1.0				
4	250	0.3	1.0				

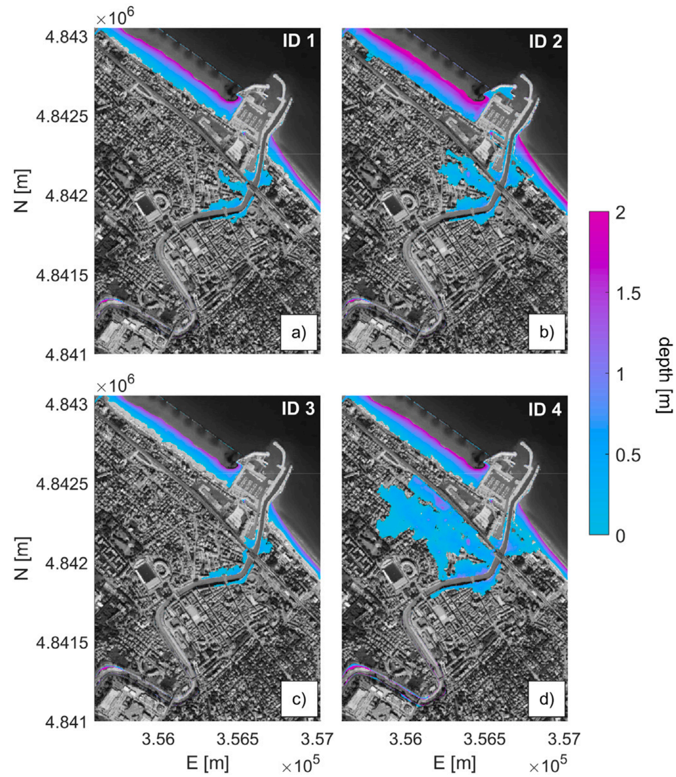

Fig. 14. Compound flooding extension due to different forcings reported in Table 2: Case 1 (a), Case 2 (b), Case 3 (c), Case 4 (d).

The highest water levels are observed along the shoreline, with significant water accumulation also occurring near the river and along the railway. Notably, when a large volume of water overtops the riverbanks before reaching the railway, the railway embankment acts as a barrier, preventing the water from draining into the sea. As a result, water levels rise further, exacerbating flooding in the affected area.

The analysis of different scenarios highlights that tide levels alone have a limited impact on flood extent within the urban area (comparison between scenarios 1 and 3). Tidal fluctuations do play a role in the inundation of coastal zones, increasing the extent of beach flooding. It should be noted that the tidal forcing used for the simulations is characterized by tidal range of 0.6 m, value that is rarely exceeded in the microtidal Misa River estuary. Despite this, the impact of the tide on the flood extent remains small if compared to the influence of other factors. A more pronounced effect is observed when storm surge levels increase (comparison between scenarios 1 and 2). A larger storm surge leads to two key consequences: (i) flooding of certain sections of the harbor area, likely due to overtopping of port infrastructure and backflow effects; (ii) an increase in flood extent both in the urban area and along the beaches. The contribution of storm surge to urban flooding is associated with its role in raising the base sea level, which in turn reduces the capacity of river discharge to drain into the sea, leading to a more extensive inundation of low-lying areas.

Among the examined drivers, the river discharge appears to have the most significant influence on urban flooding. The scenario with the highest discharge (scenario 4) results in the maximum flood extent within the urban area. This is because an increased river discharge not only raises water levels within the river channel but also enhances the likelihood of overflow and lateral flooding.

The onset of flooding is primarily controlled by the interplay between river discharge and sea levels. A key observation is that an increase in river discharge leads to an earlier initiation of flooding. This occurs because higher river discharge results in a faster rise in water levels within the channel, accelerating the overtopping or breaching of banks and the subsequent inundation of surrounding areas. In other words, when discharge rates are elevated, floodwaters propagate more rapidly, reducing the time lag between peak river flow and the onset of flooding.

In addition to river discharge, sea level variations also influence the timing of flood initiation. For a fixed river discharge, higher sea levels cause flooding to begin earlier. This is due to the fact that elevated sea levels create a backwater effect, reducing the river's ability to efficiently discharge into the sea. As a result, water accumulates more rapidly within the river system, triggering earlier flood conditions. This mechanism is particularly relevant in coastal and estuarine environments, where even moderate sea level fluctuations, due to storm surge, SLR, or tide, can significantly alter flood dynamics.

The combined effect of these factors suggests that flood risk assessment should account for both fluvial and marine contributions, as their interaction can modulate not only the flood extent but also its timing, with implications for early warning systems and flood mitigation strategies.

The presented analysis represents a preliminary evaluation of the effect of synchronous factors on the estuarine flooding. It provides information on the relative influence of river discharge and storm surge, although not accurately representing realistic or statistically based scenarios. A more in-depth analysis of the statistical occurrence of multiple factors is needed to better describe the input actions. Moreover, a more refined grid and bathymetry are needed to better represent buildings and obstacles to the flow and, consequently, reliable flooded areas.

Large-scale meteorological systems, like tropical cyclones contribute to an increasing flood hazard. This is particularly true along the coasts of Delaware, where the risk is further exacerbated by the interaction between Delaware River discharge and hurricane-induced storm surge. Kerns and Chen (2023) investigated the compound effects of rainfall, storm surge, and river discharge using a high-resolution coupled atmosphere-wave-ocean model (Unified Wave Interface-Coupled Model, UWIN-CM) along with observational data from buoys and tide gauges. Their study, focused on the flooding caused by Hurricane Irene and Tropical Storm Lee, highlighted the dominant role of storm surge in influencing flood water levels within the Delaware River. While intense rainfall combined with a moderate storm surge results in only minor flooding, a larger storm surge, even with lighter rainfall, leads to significantly more extensive flooding. This suggests that, in coastal and estuarine environments, storm surge can be the dominant driver of flooding, often outweighing the contribution of rainfall alone.

Tropical cyclone-induced flood hazards resulting from both storm tide and river discharge were also investigated by Kumbier et al. (2018). Their study focused on the low-pressure cyclone that impacted the Shoalhaven Estuary in southeastern Australia in June 2016 (Fig. 15). The findings demonstrated that a flood risk assessment considering only storm-tide flooding would have significantly underestimated the total flood extent by approximately 30%. This underscores the necessity of incorporating both fluvial and coastal contributions when evaluating flood hazards in estuarine environments. During the event, the river discharge reached $Q = 3560\ \mathrm{m^3/\ s}$, while storm surge levels at the estuary rose to 0.85 m. Offshore wave conditions were characterized by significant wave heights and peak periods of $H_s = 9$ m and $T_p = 15$ s. The storm tide played a critical role in impeding river discharge, effectively blocking its outflow and leading to an extensive flooded area of 43.5 $\mathrm{km^2}$ (see Fig. 16).

The comparison between the observed flood maps and the modeled flood maps obtained using Delft3D highlights key dynamics governing the flood extent and distribution. The analysis underscores the fundamental role of including river discharge in numerical simulations to accurately capture flooding patterns. Results reveal that upriver flooding is predominantly controlled by river discharge, as high flow rates lead to overbank flooding and water spreading across adjacent floodplains (see also for comparison Fig. 14, panel d). In contrast, flooding at the river mouth is primarily influenced by storm tide, where the combined effects of storm surge and wave setup can significantly elevate water levels, in agreement with the flooding results obtained from the numerical simulations conducted in the present study (Fig. 14). Bai et al. (2023) combined satellite and field observations with the advanced high-resolution baroclinic wave–current model (SCHISM) to investigate storm surge and flooding at the Pearl River Estuary in Shenzhen, China, during the 2017 Hato Super Typhoon, which inundated an area of 37 $\mathrm{km^2}$. Tropical cyclones increase flood hazards for Shenzhen City, a situation exacerbated by the interaction between the Pearl River discharge and Typhoon-driven surge. Numerical modeling of the Super Typhoon Hato flood using SCHISM demonstrated the major influence of the Pearl River discharge on water levels in the estuary.

All the above highlights the fundamental need to take into account sea-river and wave–current interactions for the assessment of the risk of flooding of estuarine, low-lying ares, often hosting cities, human settlements and important infrastructures.

4. Conclusions

This study highlights the crucial role of wave–current interactions in the sea-river dynamics that evolve at river mouths, particularly in microtidal environments, where the tidal forcing is relatively weak compared to other hydrodynamic drivers. These interactions significantly influence both wave dynamics and sediment transport, ultimately shaping the morphological evolution of river mouths and affecting flood dynamics.

One of the key processes observed is the modification of incoming sea-swell waves due to the presence of opposing river currents. Wave steepening, blocking, reflection, breaking, and refraction caused by these currents contribute to a filtering effect on incoming waves, altering their energy distribution. Notably, infragravity waves (IGWs) can propagate upriver, and the interaction with river currents can also induce longshore wave deflection, modifying nearshore wave patterns.

Furthermore, opposing river currents lead to the thickening of the bottom boundary layer (BBL) and an intensification of bed friction. This process enhances sediment mobilization and transport at the river mouth, resulting in the formation of larger sediment plumes and the growth of mouth bars. The evolution of these features is driven by the interplay between riverine and marine forces, where river discharge plays a dominant role in shaping mouth bars, while incoming waves tend to flatten and spread sediment plumes along the coast.

Another key finding is that flooding at river mouths is strongly dependent on the synchronicity between river discharge and storm-induced coastal water levels, including wave setup and storm surge. When high river discharge coincides with elevated sea levels, flood extent increases dramatically, exacerbating coastal inundation risks.

Fig. 15. Aerial photographs showing the flood extent of the June 2016 storm event at the Shoalhaven Estuary. Figure reproduced from Kumbier, K., Carvalho, R.C., Vafeidis, A.T. and Woodroffe, C.D., "Investigating compound flooding in an estuary using hydrodynamic modeling: a case study from the Shoalhaven River, Australia", Nat. Hazards Earth Syst. Sci., 18, 463–477, 2018, licensed under CC BY 4.0 (https://creativecommons.org/licenses/by/4.0/).

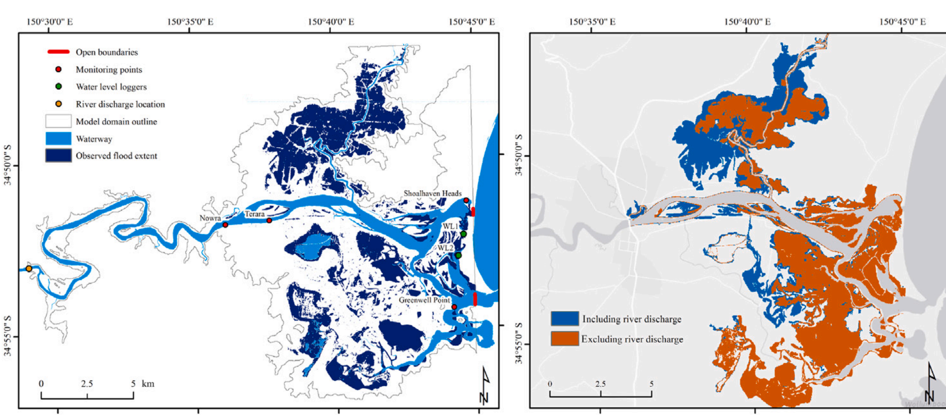

Fig. 16. The left panel shows in dark blue the flood extent of the June 2016 storm event in the lower Shoalhaven floodplain. The right panel shows the modeled maximum flood extents including (in blue) or excluding (in orange) river discharge. Figure reproduced from Kumbier, K., Carvalho, R.C., Vafeidis, A.T. and Woodroffe, C.D., "Investigating compound flooding in an estuary using hydrodynamic modeling: a case study from the Shoalhaven River, Australia", Nat. Hazards Earth Syst. Sci., 18, 463–477, 2018, licensed under CC BY 4.0 (https://creativecommons.org/licenses/by/4.0/).

This highlights the need for an integrated approach in flood hazard assessments, taking into account both fluvial and marine forcing mechanisms.

Overall, these findings emphasize the complex and interconnected nature of river-sea dynamics. A more holistic approach to estuarine flood prediction and management is needed, given the critical role of wave–current interactions. First and foremost, it is essential to properly account for the combined effects of all forcing mechanisms acting at river mouths, particularly in relation to their contribution to flooding events. This necessitates further research both on the statistical characterization of compound phenomena, such as the use of copula-based multivariate statistics involving river discharge, wave parameters, and sea levels, and on the physical mechanics of wave–current interactions, including the role of vertical current shear on wave transformation and vice versa. From an applied perspective, this improved understanding can lead to more accurate predictions, a more resilient design of coastal infrastructures and improved risk mitigation strategies. It is essential that policymakers and coastal managers consider all major drivers of estuarine flooding, particularly in low-lying areas, by integrating both hydrodynamic and morphodynamic processes into flood risk assessments and coastal management strategies.

CRediT authorship contribution statement

Maurizio Brocchini: Writing – review & editing, Supervision, Methodology, Investigation, Funding acquisition, Formal analysis, Conceptualization. **Francesco Marini:** Writing – original draft, Methodology, Investigation, Formal analysis, Data curation. **Agnese Baldoni:** Writing – original draft, Methodology, Investigation.

Declaration of competing interest

The authors declare that they have no known competing financial interests or personal relationships that could have appeared to influence the work reported in this paper.

Acknowledgments

We sincerely thank Prof. Sandro Longo and his research group for sharing photographs from an ongoing experimental study, which have been valuable for illustrating the wave blocking phenomenon. Funded under the National Recovery and Resilience Plan (NRRP), Mission 4 Component 2 Investment 1.3 - Call for tender No. 341 of 15/03/2022 of the Italian Ministry of University and Research funded by the European Union- NextGenerationEU. Award number: PE00000005, Concession Decree No. 1522 of 11/10/2022 adopted by the Italian Ministry of University and Research, D43C22003030002, “Multi-Risk sciEnce for resilienT commUnities undeR a changiNg climate” (RETURN) - Cascade funding - Spoke VS1 “Acqua”, Concession Decree No. 2812 of 9/01/2024 adopted by the General Director of Politecnico di Milano, “Mitigation and Adaptation in Resilient Coastal and estUarine integrated unitS” (MARCUS). Thanks also go to the EcoC2S Water4All EU project for partly contributing to the activities described in the present paper.

Appendix A. Supplementary data

Supplementary material related to this article can be found online at https://doi.org/10.1016/j.coastaleng.2025.104932.

Data availability

Data will be made available on request.

References

Anthony, E.J., 2015. Wave influence in the construction, shaping and destruction of river deltas: A review. Mar. Geol. 361, 53–78. http://dx.doi.org/10.1016/j.margeo.2014.12.004.

Arias, P., Bellouin, N., Coppola, E., Jones, R., Krinner, G., Marotzke, J., Naik, V., Palmer, M., Plattner, G.-K., Rogelj, J., et al., 2021. Climate Change 2021: the physical science basis. Contribution of Working Group I to the Sixth Assessment Report of the Intergovernmental Panel on Climate Change; technical summary. Technical Report.

Armstrong, J.A., Bloembergen, N., Ducuing, J., Pershan, P.S., 1962. Interactions between light waves in a nonlinear dielectric. Phys. Rev. 127, 1918–1939. http://dx.doi.org/10.1103/PhysRev.127.1918, URL: https://link.aps.org/doi/10.1103/PhysRev.127.1918.

Bai, P., Wu, L., Chen, Z., Xu, J., Li, B., Li, P., 2023. Investigating the storm surge and flooding in shenzhen city, China. Remote. Sens. 15 (20), http://dx.doi.org/10.3390/rs15205002.

Baldoni, A., Marini, F., Filomena, G., Parlani, S., Brocchini, M., 2025. Climate change-driven coastal flooding in the mid adriatic sea and adaptation of coastal defense structures. Estuar. Coast. Shelf Sci. 109535. http://dx.doi.org/10.1016/j.ecss.2025.109535.

Baldoni, A., Melito, L., Marini, F., Galassi, G., Giacomin, P., Filomena, G., Barbizzi, N., Lorenzoni, C., Brocchini, M., 2024. Modeling coastal inundation for adaptation to climate change at local scale: the case of marche region (central Italy). Front. Clim. 6, 1334625. http://dx.doi.org/10.3389/fclim.2024.1334625.

Baldoni, A., Perugini, E., Penna, P., Parlagreco, L., Brocchini, M., 2022. A comprehensive study of the river plume in a microtidal setting. Estuar. Coast. Shelf Sci. 275, 107995. http://dx.doi.org/10.1016/j.ecss.2022.107995.

Baldoni, A., Perugini, E., Soldini, L., Calantoni, J., Brocchini, M., 2021. Long-term evolution of an inner bar at the mouth of a microtidal river. Estuar. Coast. Shelf Sci. 262, 107573. http://dx.doi.org/10.1016/j.ecss.2021.107573.

Bellafiore, D., Ferrarin, C., Maicu, F., Manfè, G., Lorenzetti, G., Umgiesser, G., Zaggia, L., Levinson, A.V., 2021. Saltwater intrusion in a Mediterranean Delta under a changing climate. J. Geophys. Res.: Ocean. 126 (2), http://dx.doi.org/10.1029/2020JC016437, e2020JC016437 2020JC016437.

Bertin, X., Olabarrieta, M., 2016. Relevance of infragravity waves in a wave-dominated inlet. J. Geophys. Res.: Ocean. 121 (8), 5418–5435. http://dx.doi.org/10.1002/2015JC011444.

Bevacqua, E., Maraun, D., Vousdoukas, M.I., Voukouvalas, E., Vrac, M., Mentaschi, L., Widmann, M., 2019. Higher probability of compound flooding from precipitation and storm surge in europe under anthropogenic climate change. Sci. Adv. 5 (9), http://dx.doi.org/10.1126/sciadv.aaw5531, eaaw5531.

Bevacqua, E., Vousdoukas, M.I., Zappa, G., Hodges, K., Shepherd, T.G., Maraun, D., Mentaschi, L., Feyen, L., 2020. More meteorological events that drive compound coastal flooding are projected under climate change. Commun. Earth & Environ. 1 (1), 47. http://dx.doi.org/10.1038/s43247-020-00044-z.

Boudet, L., Sabatier, F., Radakovitch, O., 2017. Modelling of sediment transport pattern in the mouth of the rhone delta: Role of storm and flood events. Estuar. Coast. Shelf Sci. 198, 568–582. http://dx.doi.org/10.1016/j.ecss.2016.10.004.

Brevik, I., 1980. Flume experiment on waves and currents II. Smooth bed. Coast. Eng. 4, 89–110. http://dx.doi.org/10.1016/0378-3839(80)90009-5.

Chao, Y.Y., 1993. The time dependent ray method for calculation of wave transformation on water of varying depth and current. In: Ocean Wave Measurement and Analysis. ASCE, pp. 671–679.

Chawla, A., Kirby, J.T., 2002. Monochromatic and random wave breaking at blocking points. J. Geophys. Res.: Ocean. 107 (C7), http://dx.doi.org/10.1029/2001JC001042, 4–1–4–19.

Chen, Q., Madsen, P., Basco, D., 1999. Current effects on interactions of shallow water waves. J. Waterw. Port, Coast. Ocean. Eng. 125 (4), 176–186. http://dx.doi.org/10.1061/(ASCE)0733-950X(1999)125:4(176).

Chen, Q., Madsen, P.A., Schäffer, H.A., Basco, D.R., 1998. Wave-current interaction based on an enhanced Boussinesq approach. Coast. Eng. 33 (1), 11–39. http://dx.doi.org/10.1016/S0378-3839(97)00034-3.

Cooper, J., 2002. The role of extreme floods in estuary-coastal behaviour: contrasts between river-and tide-dominated microtidal estuaries. Sediment. Geol. 150 (1–2), 123–137. http://dx.doi.org/10.1016/S0037-0738(01)00271-8.

Deltares, 2025a. Delft3D-FLOW user manual: Simulation of multi-dimensional hydrodynamic flows and transport phenomena, including sediments. URL: https://content.oss.deltares.nl/delft3d4/Delft3D-FLOW_User_Manual.pdf.

Deltares, 2025b. Delft3D-WAVE User Manual: Simulation of short-crested waves with SWAN. Deltares, Delft, The Netherlands, URL: https://content.oss.deltares.nl/delft3d4/Delft3D-WAVE_User_Manual.pdf.

Deltares, 2025c. D-Flow FM User Manual: Computational cores and user interface. Deltares, Delft, The Netherlands, URL: https://content.oss.deltares.nl/delft3d/D-Flow_FM_User_Manual.pdf.

Dodet, G., 2013. Morphodynamic modelling of a wave-dominated tidal inlet: the Albufeira Lagoon (Ph.D. thesis). Université de la Rochelle.

Eldeberky, Y., 1997. Nonlinear transformation of wave spectra in the nearshore zone. Oceanograph. Lit. Rev. 4 (44), 297.

Fagherazzi, S., Edmonds, D.A., Nardin, W., Leonardi, N., Canestrelli, A., Falcini, F., Jerolmack, D.J., Mariotti, G., Rowland, J.C., Slingerland, R.L., 2015. Dynamics of river mouth deposits. Rev. Geophys. 53 (3), 642–672. http://dx.doi.org/10.1002/2014RG000451.

Flores, R.P., Williams, M.E., Horner-Devine, A.R., 2022. River plume modulation by infragravity wave forcing. Geophys. Res. Lett. 49 (15), http://dx.doi.org/10.1029/2021GL097467, e2021GL097467.

Galloway, W.E., 1975. Process framework for describing the morphologic and stratigraphic evolution of deltaic depositional systems. In: Journal of Geoscience and Environment Protection, vol. 7, pp. 87–98.

Gao, W., Shao, D., Wang, Z.B., Nardin, W., Yang, W., Sun, T., Cui, B., 2018. Combined effects of unsteady river discharges and wave conditions on river mouth bar morphodynamics. Geophys. Res. Lett. 45 (23), 12–903. http://dx.doi.org/10.1029/2018GL080447.

Garvine, R.W., 1995. A dynamical system for classifying buoyant coastal discharges. Cont. Shelf Res. 15 (13), 1585–1596. http://dx.doi.org/10.1016/0278-4343(94)00065-U, Nearshore and Coastal Oceanography.

Gerritsen, B., Goeijenbier, B., Hahury, M., Hoogerwaard, G., 2019. A predictive view on durbans flood safety.

Green, J., Haigh, I.D., Quinn, N., Neal, J., Wahl, T., Wood, M., Eilander, D., De Ruiter, M., Ward, P., Camus, P., 2025. A comprehensive review of compound flooding literature with a focus on coastal and estuarine regions. Nat. Hazards Earth Syst. Sci. 25 (2), 747–816. http://dx.doi.org/10.5194/nhess-25-747-2025.

Hasselmann, K., 1962. On the non-linear energy transfer in a gravity-wave spectrum part 1. general theory. J. Fluid Mech. 12 (4), 481–500. http://dx.doi.org/10.1017/S0022112062000373.

Huang, Z., Mei, C.C., 2003. Effects of surface waves on a turbulent current over a smooth or rough seabed. J. Fluid Mech. 497, 253–287. http://dx.doi.org/10.1017/S0022112003006657.

James, N.C., Lamberth, S.J., Midgley, C., Whitfield, A.K., 2018. Resilience of fish assemblages in the Breede Estuary, South Africa, to environmental perturbations. Environ. Biol. Fishes 101 (1), 109–126. http://dx.doi.org/10.1007/s10641-017-0685-z.

Ji, R., Yang, S.-Q., Sivakumar, M., Riaz, M.Z.B., 2025. Assessing monthly rainfall and runoff trends for sustainable water resource management in lower shoalhaven river. Discov. Water 5 (1), 20. http://dx.doi.org/10.1007/s43832-025-00200-6.

Jiménez, J., Sánchez-Arcilla, A., Valdemoro, H.I., Gracia, V., Nieto, F., 1997. Processes reshaping the Ebro delta. Mar. Geol. 144 (1–3), 59–79. http://dx.doi.org/10.1016/S0025-3227(97)00076-5.

Jonsson, I.G., Skovgaard, O., 1978. Wave refraction across a shearing current. In: Coastal Engineering 1978. pp. 722–741. http://dx.doi.org/10.1061/9780872621909.043.

Kemp, P.H., Simons, R.R., 1982. The interaction between waves and a turbulent current: waves propagating with the current. J. Fluid Mech. 116, 227–250, URL: https://api.semanticscholar.org/CorpusID:123424791.

Kemp, P.H., Simons, R.R., 1983. The interaction of waves and a turbulent current: waves propagating against the current. J. Fluid Mech. 130, 73–89. http://dx.doi.org/10.1017/S0022112083000981.

Kerns, B., Chen, S., 2023. Compound effects of rain, storm surge, and river discharge on coastal flooding during hurricane irene and tropical storm lee (2011) in the mid-atlantic region: coupled atmosphere-wave-ocean model simulation and observations.. Nat. Hazards 116, 693–726. http://dx.doi.org/10.1007/s11069-022-05694-0.

Kumar, A., Hayatdavoodi, M., 2023. On wave–current interaction in deep and finite water depths. J. Ocean. Eng. Mar. Energy 9 (3), 455–475. http://dx.doi.org/10.1007/s40722-023-00278-x.

Kumbier, K., Carvalho, R.C., Vafeidis, A.T., Woodroffe, C.D., 2018. Investigating compound flooding in an estuary using hydrodynamic modelling: a case study from the shoalhaven river, Australia. Nat. Hazards Earth Syst. Sci. 18 (2), 463–477. http://dx.doi.org/10.5194/nhess-18-463-2018, URL: https://nhess.copernicus.org/articles/18/463/2018/.

Kupfer, S., Santamaria-Aguilar, S., van Niekerk, L., Lück-Vogel, M., Vafeidis, A.T., 2022. Investigating the interaction of waves and river discharge during compound flooding at Breede Estuary, South Africa. Nat. Hazards Earth Syst. Sci. 22 (1), 187–205. http://dx.doi.org/10.5194/nhess-22-187-2022.

Levin, D.R., 1993. Tidal inlet evolution in the mississippi river delta plain. J. Coast. Res. 462–480.

Li, X., Cai, Y., Liu, Z., Mo, X., Zhang, L., Zhang, C., Cui, B., Ren, Z., 2023. Impacts of river discharge, coastal geomorphology, and regional sea level rise on tidal dynamics in Pearl River Estuary. Front. Mar. Sci. 10, 1065100. http://dx.doi.org/10.3389/fmars.2023.1065100.

Liu, B., Peng, S., Liao, Y., Wang, H., 2019. The characteristics and causes of increasingly severe saltwater intrusion in Pearl River Estuary.. Estuar. Coast. Shelf Sci. 220, 54–63.

Lodahl, C.R., Sumer, B.M., Fredsøe, J., 1998. Turbulent combined oscillatory flow and current in a pipe. J. Fluid Mech. 373, 313–348. http://dx.doi.org/10.1017/S0022112098002559.

Lyddon, C., Chien, N., Vasilopoulos, G., Ridgill, M., Moradian, S., Olbert, A., Coulthard, T., Barkwith, A., Robins, P., 2024. Thresholds for estuarine compound flooding using a combined hydrodynamic–statistical modelling approach. Nat. Hazards Earth Syst. Sci. 24 (3), 973–997. http://dx.doi.org/10.5194/nhess-24-973-2024, URL: https://nhess.copernicus.org/articles/24/973/2024/.

Maillet, G.M., Poizot, E., Sabatier, F., Vella, C., Méar, Y., 2011. Pattern of sediment transport in a microtidal river mouth using geostatistical sediment-trend analysis. J. Sediment. Res. 81 (2), 138–152. http://dx.doi.org/10.2110/jsr.2011.8.

McKeon, K., Piecuch, C.G., 2025. Compound minor floods and the role of discharge in the Delaware River Estuary. J. Geophys. Res.: Ocean. 130 (3), e2024JC021716.

Melito, L., Postacchini, M., Sheremet, A., Calantoni, J., Zitti, G., Darvini, G., Penna, P., Brocchini, M., 2020. Hydrodynamics at a microtidal inlet: Analysis of propagation of the main wave components. Estuar. Coast. Shelf Sci. 235, 106603. http://dx.doi.org/10.1016/j.ecss.2020.106603.

Mikhailov, V., Mikhailova, M., 2010. Delta formation processes at the mississippi river mouth. Water Resour. 37 (5), 595–610. http://dx.doi.org/10.1134/S0097807810050015.

Muñoz, D., Moftakhari, H., Moradkhani, H., 2020. Compound effects of flood drivers and wetland elevation correction on coastal flood hazard assessment. Water Resour. Res. 56 (7), http://dx.doi.org/10.1029/2020WR027544, e2020WR027544.

Nienhuis, J.H., Ashton, A.D., Giosan, L., 2015. What makes a delta wave-dominated? Geology 43 (6), 511–514. http://dx.doi.org/10.1130/G36518.1.

Olabarrieta, M., Medina, R., Castanedo, S., 2010. Effects of wave–current interaction on the current profile. Coast. Eng. 57 (7), 643–655. http://dx.doi.org/10.1016/j.coastaleng.2010.02.003.

Osadchiev, A., Zavialov, P., 2019. Structure and dynamics of plumes generated by small rivers. In: Pan, J., Devlin, A. (Eds.), Estuaries and Coastal Zones - Dynamics and Response To Environmental Changes. IntechOpen, Rijeka, http://dx.doi.org/10.5772/intechopen.87843.

Peregrine, D., 1976. Interaction of water waves and currents. In: Yih, C.-S. (Ed.), Advances in Applied Mechanics. vol. 16, Elsevier, pp. 9–117. http://dx.doi.org/10.1016/S0065-2156(08)70087-5.

Peregrine, D., Jonsson, I., 1983. Interaction of Waves and Currents. In: Miscellaneous report, U.S. Coastal Engineering Research Center, URL: https://books.google.it/books?id=zHi4zwEACAAJ.

Phillips, O.M., 1960. On the dynamics of unsteady gravity waves of finite amplitude part 1. the elementary interactions. J. Fluid Mech. 9 (2), 193–217. http://dx.doi.org/10.1017/S0022112060001043.

Postacchini, M., Manning, A.J., Calantoni, J., Smith, J.P., Brocchini, M., 2023. A storm driven turbidity maximum in a microtidal estuary. Estuar. Coast. Shelf Sci. 288, 108350. http://dx.doi.org/10.1016/j.ecss.2023.108350.

Rautenbach, C., Daniels, T., de Vos, M., Barnes, M.A., 2020. A coupled wave, tide and storm surge operational forecasting system for South Africa: validation and physical description. Nat. Hazards 103 (1), 1407–1439. http://dx.doi.org/10.1007/s11069-020-04042-4.

Roco, A., Flores, R.P., Williams, M.E., Saldías, G.S., 2024. Observations of river-wave interactions at a small-scale river mouth. Coast. Eng. 189, 104456. http://dx.doi.org/10.1016/j.coastaleng.2024.104456.

Sabatier, F., Anthony, E., 2015. The sand spits of the rhone river delta: Formation, dynamics, sediment budgets and management. In: Sand and Gravel Spits. Springer, pp. 259–274. http://dx.doi.org/10.1007/978-3-319-13716-2_14.

Sabatier, F., Samat, O., Ullmann, A., Suanez, S., 2009. Connecting large-scale coastal behaviour with coastal management of the rhone delta. Geomorphology 107 (1–2), 79–89. http://dx.doi.org/10.1016/j.geomorph.2006.09.026.

Sioni, F., Davolio, S., Grazzini, F., Giovannini, L., 2023. Revisiting the atmospheric dynamics of the two century floods over north-eastern Italy. Atmos. Res. 286, 106662. http://dx.doi.org/10.1016/j.atmosres.2023.106662.

Sorourian, S., Huang, H., Li, C., Justic, D., Payandeh, A.R., 2020. Wave dynamics near barataria bay tidal inlets during spring–summer time. Ocean. Model. 147, 101553. http://dx.doi.org/10.1016/j.ocemod.2019.101553.

Suastika, K., 2004. Wave blocking. Commun. Hydraul. Geotech. Eng. 4 (4), i–154.

Tambroni, N., Blondeaux, P., Vittori, G., 2015. A simple model of wave–current interaction. J. Fluid Mech. 775, 328–348. http://dx.doi.org/10.1017/jfm.2015.308.

Umeyama, M., 2005. Reynolds stresses and velocity distributions in a wave-current coexisting environment. J. Waterw. Port, Coast. Ocean. Eng. 131 (5), 203–212. http://dx.doi.org/10.1061/(ASCE)0733-950X(2005)131:5(203).

Uncles, R., Stephens, J., Harris, C., 2014. Infragravity currents in a small ría: Estuary-amplified coastal edge waves? Estuar. Coast. Shelf Sci. 150, 242–251. http://dx.doi.org/10.1016/j.ecss.2014.04.019, Special issue on Problems of Small Estuaries.

Valle-Levinson, A., 2010. Definition and classification of estuaries. In: Contemporary Issues in Estuarine Physics. Cambridge University Press, pp. 1–11.

Wahl, T., Jain, S., Bender, J., Meyers, S.D., Luther, M.E., 2015. Increasing risk of compound flooding from storm surge and rainfall for major US cities. Nat. Clim. Chang. 5 (12), 1093–1097. http://dx.doi.org/10.1038/nclimate2736.

van der Westhuysen, A.J., 2012. Spectral modeling of wave dissipation on negative current gradients. Coast. Eng. 68, 17–30. http://dx.doi.org/10.1016/j.coastaleng.2012.05.001.

Winckler, P., Contreras-López, M., Campos-Caba, R., Beyá, J.F., Molina, M., 2017. The storm of august 8, 2015 in the regions of valparaíso and coquimbo, central Chile. Lat. Am. J. Aquat. Res. 45 (4), 622–648. http://dx.doi.org/10.3856/vol45-issue4-fulltext-1.

Xiao, Z., Yang, Z., Wang, T., Sun, N., Wigmosta, M., Judi, D., 2021. Characterizing the non-linear interactions between tide, storm surge, and river flow in the delaware Bay Estuary, United States. Front. Mar. Sci. 8, 715557. http://dx.doi.org/10.3389/fmars.2021.715557.

Yankovsky, A.E., Chapman, D.C., 1997. A simple theory for the fate of Buoyant Coastal discharges. J. Phys. Oceanogr. 27 (7), 1386–1401. http://dx.doi.org/10.1175/1520-0485(1997)027<1386:ASTFTF>2.0.CO;2.

Yuxing, W., Ting, G., Ning, J., Zhenyu, H., 2020. Numerical study of the impacts of typhoon parameters on the storm surge based on hato storm over the pearl river mouth, China. Reg. Stud. Mar. Sci. 34, 101061. http://dx.doi.org/10.1016/j.rsma.2020.101061.

Zăinescu, F., Anthony, E., Vespremeanu-Stroe, A., 2021. River jets versus wave-driven longshore currents at river mouths. Front. Mar. Sci. 8, 708258. http://dx.doi.org/10.3389/fmars.2021.708258.

Zăinescu, F., Storms, J.E., Vespremeanu-Stroe, A., Van Der Vegt, H., Schuster, M., Anthony, E., 2024. Wave-influenced delta morphodynamics, long-term sediment bypass and trapping controlled by relative magnitudes of riverine and wave-driven sediment transport. Geophys. Res. Lett. 51 (19), http://dx.doi.org/10.1029/2024GL111069, e2024GL111069.

Zhang, G., Chen, Y., Cheng, W., Zhang, H., Gong, W., 2021. Wave effects on sediment transport and entrapment in a channel-shoal estuary: The Pearl River Estuary in the dry winter season. J. Geophys. Res.: Ocean. 126 (4), http://dx.doi.org/10.1029/2020JC016905, e2020JC016905.

Zscheischler, J., Martius, O., Westra, S., Bevacqua, E., Raymond, C., Horton, R.M., van den Hurk, B., AghaKouchak, A., Jézéquel, A., Mahecha, M.D., et al., 2020. A typology of compound weather and climate events. Nat. Rev. Earth & Environ. 1 (7), 333–347. http://dx.doi.org/10.1038/s43017-020-0060-z.